

# Influence of radial transport and turbulent effects on CO<sub>2</sub> conversion in a microwave plasma reactor: Insights from a multi-dimensional thermo-chemical flow model.

Helder M.S. Van Poyer, Ivan Tsonev, Stein J.R. Maerivoet, Matthias C.K. Albrechts, Annemie Bogaerts

Research Group PLASMANT, Department of Chemistry, University of Antwerp, Universiteitsplein 1, BE-2610 Wilrijk-Antwerp, Belgium

## Abstract

We developed a thermo-chemical 2D axisymmetric model, describing turbulent fluid dynamics, heat transfer, species transport and chemistry, to gain insight into the fundamental mechanisms of CO<sub>2</sub> conversion in MW plasmas. We validated our model against experiments for a range of flow rates (10-40 slm) and specific energy inputs (0.4-2.1 eV molecule<sup>-1</sup>) at atmospheric pressure, for straight tube experiments without constriction. We performed spatially dependent reaction analysis to assess the spatial dependence of CO<sub>2</sub> conversion within the reactor, showing that net CO production happens at the edge of the plasma. Importantly, in contrast to assumptions in literature, net production and destruction rates do not balance each other, due to the radial diffusion of species. Furthermore, we investigated the effect of turbulence on the temperature profile, by comparing turbulent and laminar flow profiles. The additional turbulent thermal conductivity and turbulent diffusion lead to increased heat loss through the reactor walls. Overall, our model indicates the need for including radial diffusion and turbulence in multi-dimensional models of CO<sub>2</sub> MW plasmas. Finally, our model predicts that at high flow rates (40 slm), turbulent diffusion may be a key driver for net CO transport into the cold gas stream at the reactor edges, after which it is convectively transported to the outlet. We hypothesize based on our calculations that by enhancing the turbulent effects, upon changing reactor design or gas flow dynamics, the net transport of the produced CO towards the cold edge of the reactor could be further promoted, increasing the overall CO<sub>2</sub> conversion.

## Keywords

Plasma; CO<sub>2</sub>; Computational fluid dynamics; Diffusion; Turbulence.

## 1. Introduction

Over the past three decades, the atmospheric CO<sub>2</sub> concentration has risen by over 30%, presenting a major challenge to the scientific community to provide technologies that can lower this concentration [1]. The growing adoption of renewable energy can help reduce carbon emissions associated with energy production [2]. However, the non-energy utilization of fossil fuels remains a significant contributor to CO<sub>2</sub> emissions [3]. Therefore, carbon capture and utilization (CCU) pathways have been explored as potential solutions to reduce CO<sub>2</sub> emissions [4]. This paper focuses on the conversion of CO<sub>2</sub> into CO and O<sub>2</sub>, where CO can be used as essential feedstock for synthesizing a variety of fuels and chemicals [5, 6]. Thermodynamically, this reaction has a specific energy requirement of 2.93 eV per dissociated CO<sub>2</sub> molecule at 400 K and atmospheric pressure, if the potential energy of the formed oxygen atom (CO<sub>2</sub> + M → CO + O + M) is reinvested into dissociating additional CO<sub>2</sub> (CO<sub>2</sub> + O → CO + O<sub>2</sub>) [7].

Plasma technology finds interest in various industrial applications, e.g. spray coating, treating toxic waste, and surface modification [8, 9]. In recent decades, there has been increasing interest in leveraging this technology for the conversion of CO<sub>2</sub>, primarily due to its quick on-off capabilities, which facilitates the storage of fluctuating energy [10, 11]. Both conversion and energy efficiency are typically used to gauge performance of plasma-based CO<sub>2</sub> dissociation [12]. Microwave (MW) plasma reactors are regarded as one of the most promising paths for plasma-based CO<sub>2</sub> conversion, due to their capacity for highly efficient conversion and the absence of electrodes, which reduces the need for maintenance, a crucial consideration for industrial feasibility [7, 10-17].

In recent years, great strides were made in demonstrating that thermal dissociation is the dominant mechanism as the driver of conversion and energy efficiency in high-pressure MW CO<sub>2</sub> plasmas [7, 10, 14, 18-20]. den Harder et al. compared the experimentally measured temperature and conversion with a zero-dimensional (0D) model that assumes thermal composition, and concluded that the measured gas temperatures and net CO production are consistent with net production due to thermal quenching [18]. Additionally, various authors found that the rotational and vibrational temperature are equal, by fitting the temperature of the C<sub>2</sub> Swan band [14, 18-20]. Hence, there is both experimental and computational evidence that CO<sub>2</sub> dissociation in MW plasmas near atmospheric pressure is predominantly thermal [7, 10, 14].

In addition, van de Steeg et al. conducted spatially resolved Raman spectroscopy to map the spatial concentrations of species within CO<sub>2</sub> MW plasma, although neglecting C atoms, and concluded, by combining the experimental data with a 0D kinetics model, that fast transport of species along the temperature gradient allows for additional net CO production upon diffusion of O atoms [20, 21].

Multiple multi-dimensional models have been developed for CO<sub>2</sub> plasma reactors [5, 15, 22-24]. Several of these models solved for non-isothermal flow in higher dimensions under the assumption of local thermodynamic equilibrium (LTE), not accounting for diffusion due to the high gradients at the edge of the plasma, which may alter the thermophysical properties (heat capacity, thermal conductivity, and dynamic viscosity) of the fluid, as well as cause deviations in chemical equilibrium [22, 23]. LTE requires that a detailed equilibrium is achieved between each collision process and its reverse process [25]. Additionally, for LTE to hold, local gradients in plasma properties, such as temperature and density, must be sufficiently small. This ensures that any plasma species diffusing from one location to another within the plasma has enough time to equilibrate [25].

Furthermore, not all multi-dimensional models account for turbulence [5, 15, 26]. For instance, Wang et al. solved for laminar flow, but when accounting for additional cooling, which was assumed to arise from turbulence, they could predict more accurate temperature profiles within the reactor [5]. Moreover,

Elahi et al. developed a fully coupled 2D computational model of a CO<sub>2</sub> microwave plasma diluted with argon, assuming laminar flow. They overestimated the outlet gas temperature, while obtaining good agreement with measured conversion [27]. Indeed, as we will discuss in this paper, the turbulent flow adds turbulent diffusion and turbulent thermal conductivity, increasing the overall heat transfer, which can be quite important and should not be neglected. Furthermore, Wolf et al. approximated the turbulent viscosity in 2D as an analytic expression dependent on the radial position. They found reasonable agreement with experimental trends, but indicated that a more accurate description of turbulent kinematic viscosity would improve the model [15].

While the plasma chemistry of CO<sub>2</sub> conversion can be quite complex [28-31], in atmospheric pressure MW plasmas it can be reduced to thermal chemistry, which is experimentally found to be dominant in determining conversion [5, 14, 15, 19, 20], and this was also confirmed by modeling [10, 26, 32, 33]. Moreover, Vermeiren et al. compared plasma-based conversion and thermal conversion by means of chemical kinetics modelling and reported that for temperatures above 3000 K the conversion is mostly thermal [32]. In literature this reactor was previously modelled by Van Alphen et al. and Kotov et al [22, 33]. Most recently, Kotov et al. published a 1.5 D model in order to validate the thermo-chemical approach, and they found that radial diffusion of both CO and O leads to increased conversion of CO, as well as local increases in reoxidation of CO [33]. Kotov's model did not account for the effect of vortex stabilization on the bulk flow and the effect of turbulence on species transport. They mentioned the need for developing a more comprehensive model that includes vortex flow to validate their findings. Therefore, in our paper, we present an improved 2D axisymmetric model, accounting for the limitations of the model in [33]. It must be noted that a precessing helical vortex cannot be captured in 2D-axisymmetric models, which may locally influence the heat transfer coefficient, which in turn may influence the mass transfer [34, 35]. Nevertheless, Tatar et al. have recently published a 3D model for air plasmas, with the results being largely axisymmetric, justifying our 2D axisymmetric approach [36].

Specifically, our paper aims to increase our understanding of fluid dynamics and species transport effects in CO<sub>2</sub> MW plasma reactors, by building a 2D axisymmetric thermo-chemical flow model at atmospheric pressure. Please note that a 2D axisymmetric model results in a slice of a 3D solution, without any gradients in the  $\phi$ -direction. When the slice is revolved around the symmetry axis, the solution becomes a 3D field.

First, we will validate our model, showing that CO<sub>2</sub> conversion in MW plasmas can be predicted reasonably well, based on experimental results of D'Isa et al. [7]. Moreover, we will illustrate the need for coupling all physics considered in the model, by emphasizing the significance of species transport, i.e., diffusion towards and from the edges of the plasma. Finally, we will show based on our theoretical results that at high flow rates (40 slm) turbulent cooling and turbulent diffusion may play a significant role in determining the temperature profile and conversion.

## 2. Model description

To reveal the influence of the flow pattern and species transport inside the plasma and effluent (i.e., afterglow), we developed a 2D axisymmetric reacting flow model that calculates gas flow velocity, temperature profiles, transport of species and chemistry self-consistently inside the MW plasma reactor within COMSOL Multiphysics 6.2. We will first specify the geometry of the computational domain and our methodology for translating 3D gas flow data into a 2D axisymmetric model. Subsequently, we will provide the equations used to describe the various physical phenomena within the 2D axisymmetric framework. Finally, we will list the boundary conditions for the various models. The model was solved using the fully coupled PARADISO Automatic Newton solver with a relative tolerance of 0.001. The model was solved on an intel i9-13900k with 128 GB of DDR4 RAM.

### 2.1. Reactor geometry: 3D and 2D axisymmetric representation

The reactor geometry considered in this work is the one described by D’Isa et al. [7], as we use their experimental data for model validation. It needs to be noted that most experiments were conducted at 900 mbar, whereas the model is calculated at atmospheric pressure, but the 900 mbar is taken as a proxy for atmospheric pressure. This is a reasonable approximation given that Hecimovic et al. reported that conversion becomes less pressure dependent with increasing pressure and within the error bars above 800 mbar, for 5 slm in the same reactor [37]. The geometry is presented in Figure 1, with the inlets indicated in both the reactor drawing and the 3D geometry. At the base of the coaxial resonator, gas is introduced into the (26 mm inner diameter) quartz tube via four (4.3 mm diameter) tangential gas inlets. The quartz tube has a length of 400 mm (but only part of it is shown in the left and middle panel of Figure 1). The tip features two geometric sections: a cylinder with dimensions of 15 mm in diameter and 12 mm in height, and a cone with a height of 8 mm and the same base diameter of 15 mm [7].

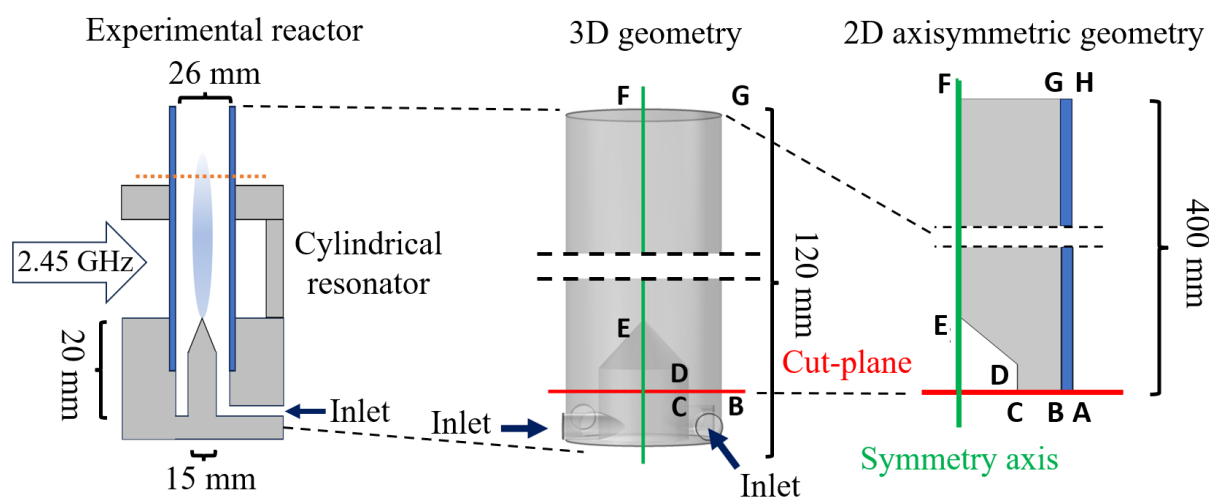


Figure 1. Left: Schematic drawing of the experimental reactor, as described by d’Isa et al. [7], and how it is translated into the 3D (middle) as well as the 2D geometry (right). The boundaries are indicated by letters for both the 3D and 2D axisymmetric geometry (see section 2.6 below). The orange dotted line in the left figure indicates the position at which the calculated and measured radial temperature profile are compared, cf. section 3.1 below). The red line in the middle and right figure indicates the cut plane in which the 3D velocity profile is translated into the 2D axisymmetric domain, to represent the 2D gas velocity profile at the inlet for the 2D model. The green line indicates the symmetry axis in the 2D geometry.

As the thermo-chemical model is computationally too expensive to solve in 3D, we only calculate the gas flow velocity in 3D. The 3D velocity profile of the cut plane (indicated in red in the left and right panel of Figure 1) is translated into the 2D axisymmetric coordinates, to represent the 2D axisymmetric gas velocity profile at the inlet for the 2D axisymmetric model. This operation is based on the relations for converting Cartesian coordinates into cylindrical coordinates [38, 39]:

$$v_r = \frac{xv_x + yv_y}{\sqrt{x^2 + y^2}} \quad (1)$$

$$v_\phi = \frac{xv_y - yv_x}{\sqrt{x^2 + y^2}} \quad (2)$$

$$v_z = v_z \quad (3)$$

With  $v_j$  the different velocity components and  $(x, y, z)$  the Cartesian coordinate positions.

The velocity components are averaged over the  $\phi$ -direction at the cut plane, indicated by the red line in Figure 1, thus making the velocity profile dependent on the radial position at the inlet in the 2D axisymmetric domain. The 3D model is thus computed to obtain a boundary condition at the inlet of the 2D axisymmetric model, as done by Maerivoet et al. [39]. Mass is conserved in this transition within a 3% variation, since the identical temperature at the inlet ensures equal densities.

The plasma acts as a heat source, the size of which is dependent on the input power, digitized from measurements by D'isa et. al. for all considered conditions [7] (see Supplementary Information (SI), section S.1, Figure S.1). However, the power density distribution is not accurately known. Therefore, we performed a sensitivity analysis on the shape of the heat source, as will be discussed in section 3.2 below. In first approximation, we take the power density distribution as a rectangular function along the axial direction and a normalized Gaussian function along the radial direction, as illustrated in Figure 2. The value of  $x$  corresponds to two standard deviations of the Gaussian function. The values of  $x$  and  $y$  depend on the input power and are represented for different input powers in the SI (section S.1, Figure S.1).

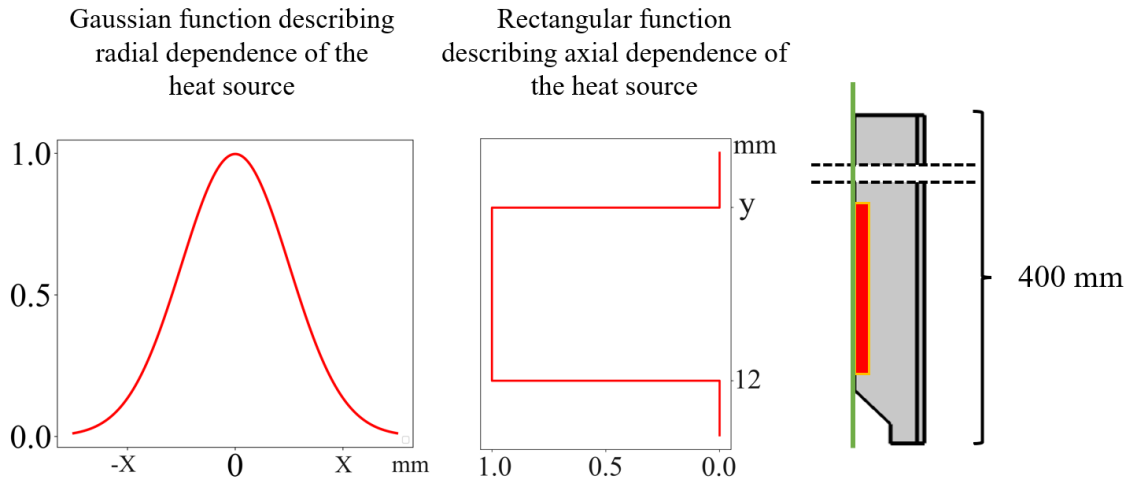


Figure 2. Gaussian function representing the radial power distribution (left) and rectangular function describing the axial power distribution (middle). The plasma size is measured for each condition by d'Isa et al., determining the values of  $x$  and  $y$  in this figure [7]. The shape of the heat source is schematically illustrated in the right figure.

The quartz tube, indicated in blue in Figure 1 (and domain (ABGH) in the right panel) has a temperature-dependent thermal conductivity and heat capacity, taken from the NIST Standard reference material database [40]. The meshes used in the simulations are detailed in the SI (section S.2, Figure S.2), for both the 3D and 2D axisymmetric mesh. The thermophysical properties of the quartz tube are also presented in SI (section S.3, Figure S.4).

## 2.2. Fluid dynamics in 3D and 2D axisymmetric geometry

We describe the gas flow behavior using a Reynolds-Averaged Navier Stokes (RANS) Menter's Shear Stress Transport (SST) turbulent gas flow model. The SST model combines both the  $k$ - $\epsilon$  and  $k$ - $\omega$  model, effectively removing the empirical damping functions at the near-wall regions employed by the  $k$ - $\epsilon$  model, furthermore when the SST turbulence model is employed, the turbulent viscosity goes to zero when the turbulent kinetic energy goes to zero. This model solves the mass continuity and momentum continuity equations for a Newtonian fluid [41, 42]:

$$\nabla \cdot (\rho \mathbf{u}) = 0 \quad (4)$$

$$\rho(\mathbf{u} \cdot \nabla) \mathbf{u} = \nabla \cdot \left[ -p \mathbf{I} + (\mu + \mu_T)(\nabla \mathbf{u} + (\nabla \mathbf{u})^T) - \frac{2}{3}(\mu + \mu_T)(\nabla \cdot \mathbf{u}) \mathbf{I} - \frac{2}{3}(\rho k) \mathbf{I} \right] \quad (5)$$

Where  $\rho$  stands for the gas density ( $\text{kg m}^{-3}$ ),  $\mathbf{u}$  for the gas flow velocity ( $\text{m s}^{-1}$ ),  $p$  is the gas pressure (Pa),  $\mathbf{I}$  is the unity tensor,  $\mu$  is the molecular dynamic viscosity (Pa s) and  $\mu_T$  the turbulent viscosity (Pa s), superscript T stands for transposition, and  $k$  is the turbulent kinetic energy ( $\text{m}^2 \text{s}^{-2}$ ). The calculation of the turbulent viscosity is added in the SI (section S.4, equations 1-4).

The governing equations for the turbulent kinetic energy, which represents the energy associated with turbulent fluctuations, and for the specific dissipation rate  $\omega$  ( $\text{s}^{-1}$ ), which quantifies the rate at which turbulent kinetic energy is dissipated into heat due to viscous effects, are given by [43]:

$$\rho(\mathbf{u} \cdot \nabla) k = \nabla \cdot ((\mu + \mu_T \sigma_k) \nabla k) + P - \beta_o \rho \omega k \quad (6)$$

$$\rho(\mathbf{u} \cdot \nabla) \omega = \nabla \cdot ((\mu + \mu_T \sigma_\omega) \nabla \omega) + \frac{\gamma}{\mu_T} \rho P - \beta \rho \omega^2 + 2(1 - f_{v1}) \frac{\sigma_{\omega 2} \rho}{\omega} \nabla k \cdot \nabla \omega \quad (7)$$

Here  $P$  is the turbulent kinetic energy source term,  $\beta_o$  and  $\sigma_{\omega 2}$  are turbulence modelling parameters,  $\gamma$ ,  $\beta$ ,  $\sigma_k$  and  $\sigma_\omega$  are turbulence parameters depending on blending function  $f_{v1}$ . The blending function,  $f_{v1}$ , and the values for the variables used are presented in the SI (section S.4, equations 5-7).

### 2.3. Transport of species

The transport of the various species within the plasma is described using the conservation of mass equation:

$$\nabla \cdot \mathbf{J}_i + \rho(\mathbf{u} \cdot \nabla)\xi_i = R_i \quad \text{with} \quad R_i = \sum_j R_{ij} \quad (8)$$

Here,  $\mathbf{J}_i$  is the diffusive flux vector of species  $i$  ( $\text{kg m}^{-2} \text{s}^{-1}$ ),  $\xi_i$  is the weight fraction of species  $i$ , and  $R_i$  is the total net production rate of species  $i$  ( $\text{kg m}^{-3} \text{s}^{-1}$ ). The species included in this model are  $\text{CO}_2$ ,  $\text{CO}$ ,  $\text{O}_2$ ,  $\text{C}$  and  $\text{O}$ .

The diffusive flux is obtained from the mixture-averaged diffusion model, assuming isobaric conditions [44, 45]:

$$\mathbf{J}_i = - \left( \rho D_i^m \nabla \xi_i + \rho \xi_i D_i^m \frac{\nabla M_n}{M_n} - \mathbf{J}_{c,i} + \mathbf{J}_{T,i} \right) \quad (9)$$

Here,  $D_i^m$  is the diffusion coefficient for species  $i$  ( $\text{m}^2 \text{s}^{-1}$ ),  $M_n$  is the mean molar mass ( $\text{kg mol}^{-1}$ ),  $\mathbf{J}_{c,i}$  is the multi-component diffusive flux correction term ( $\text{kg m}^{-2} \text{s}^{-1}$ ). For further explanation regarding this term, we refer to [46].  $\mathbf{J}_{T,i}$  is the turbulent diffusive flux vector ( $\text{kg m}^{-2} \text{s}^{-1}$ ). Neglecting the pressure term is a reasonable approximation, given that in the calculations the minimum pressure never drops below 99.9% of the maximum pressure

$D_i^m$ ,  $M_n$ ,  $\mathbf{J}_{c,i}$  and  $\mathbf{J}_{T,i}$  are calculated via [47]:

$$\rho = \frac{p M_n}{R_g T} \quad (10)$$

$$D_i^m = \frac{1 - \xi_i}{\sum_{j \neq i} \frac{x_j}{D_{i,j}}} \quad (11)$$

$$D_{ij} = 2.628 \times 10^{-22} \sqrt{\frac{T^3(M_i + M_j)/(2 \times 10^3(M_i M_j))}{p \sigma_i \sigma_j \Omega_D}} \quad (12)$$

$$\Omega_D = \frac{c_1}{(T^*)^{c_2}} + \frac{c_3}{\exp(c_4 T^*)} + \frac{c_5}{\exp(c_6 T^*)} + \frac{c_7}{k_b^2 T^* \sigma_i^6}, \quad T^* = T \frac{k_b}{\sqrt{\varepsilon_i \varepsilon_j}} \quad (13)$$

$$M_n = \left( \sum_i \frac{\xi_i}{M_i} \right)^{-1} \quad (14)$$

$$\mathbf{J}_{c,i} = \rho \xi_i \sum_k \frac{M_i}{M_n} D_k^m \nabla x_k \quad (15)$$

$$\mathbf{J}_{T,i} = \rho \xi_i D_{T,i} \nabla \xi_i \quad (16)$$

$$D_{T,i} = \frac{v_T}{Sc_T} \quad (17)$$

$$Sc_T = \left( \frac{1}{2 Sc_{T\infty}} + \frac{0.3 Pe_T}{\sqrt{Sc_{T\infty}}} - (0.3 Pe_T)^2 \left( 1 - e^{-1/(0.3 Pe_T \sqrt{Sc_{T\infty}})} \right) \right)^{-1} \quad (18)$$

Here  $R_g$  ( $\text{J mol}^{-1} \text{K}^{-1}$ ) represents the ideal gas constant.  $x_k$  represents the mole fraction of species  $i$ ,  $D_{i,j}$  is the binary diffusion coefficient ( $\text{m}^2 \text{s}^{-1}$ ),  $\sigma_j$  (m) the characteristic length of the Lennard-Jones/Stockmayer potential,  $\Omega_D$  the dimensionless collision integral and  $c_x$  are empirical constants, reported by Neufeld et al. [47].  $M_i$  is the molar mass of species  $i$  ( $\text{kg mol}^{-1}$ ),  $D_{T,i}$  is the turbulent diffusion coefficient of species  $i$  ( $\text{m}^2 \text{s}^{-1}$ ),  $v_T$  is the turbulent kinematic viscosity ( $\text{m}^2 \text{s}^{-1}$ ) and  $Sc_T$  is the

turbulent Schmidt number, calculated according to the Kays-Crawford model with  $Sc_{T^\infty} = 0.85$ , and  $Pe_T$  is the turbulent Peclet number [48].

## 2.4. Chemistry included in the model

As mentioned above, the species included in the model are  $CO_2$ ,  $CO$ ,  $O_2$ ,  $C$  and  $O$ . They interact in 6 reversible chemical reactions, tabulated in Table 1. The reverse rates are calculated using detailed balancing.

**Table 1 Reactions included in the model with their forward reaction rate coefficients. The reverse rate coefficients are calculated by the principle of detailed balancing. M stands for any of the five species included in the model. The forward rate coefficients are denoted in  $cm^3 mol^{-1} s^{-1}$  for two-body reactions and in  $cm^6 mol^{-2} s^{-1}$  for three-body reactions. All reactions are written with  $CO$  as reaction product for clarity. However, for reaction R2 the reverse rate coefficient is tabulated ( $k_r$ ), because this reaction is typically presented in literature with  $CO$  as reactant, and thus, here the forward rate coefficient ( $k_f$ ) is calculated by detailed balancing.**

No.	Reaction	Reaction rate coefficient	Ref.
R1	$CO_2 + M \rightleftharpoons CO + O + M$	$C_{eff1} = 6c_{CO_2} + 1.5c_{CO} + 3.5c_{CO_2} + 1c_O + 1c_c$ $k_{01} = 6.02 \times 10^{14} [cm^6 mol^{-2} s^{-1}] \times e^{\left(\frac{-1509[K]}{T}\right)}$ $k_{inf1} = 1.80 \times 10^{10} [cm^3 mol^{-1} s^{-1}] \times e^{\left(\frac{1205[K]}{T}\right)}$ $k_{r1} = \frac{k_{inf1}}{1 + k_{inf1}/k_{01} \times C_{eff1}}$ $T_{range} = 300-3500 \text{ K}$	[49]
R2	$CO_2 + O \rightleftharpoons CO + O_2$	$k_{r2} = 2.50 \times 10^{12} [cm^3 mol^{-1} s^{-1}] \times e^{\left(\frac{-24106[K]}{T}\right)}$ $T_{range} = 1500-3000 \text{ K}$	[49]
R3	$C + O_2 \rightleftharpoons CO + O$	$k_{f3} = 5.80 \times 10^{13} [cm^3 mol^{-1} s^{-1}] \times e^{\left(\frac{-290[K]}{T}\right)}$ $T_{range} = 300-4200 \text{ K}$	[49]
R4	$O + O + M \rightleftharpoons O_2 + M$	$C_{eff4} = 1.75c_{CO} + 3.6c_{CO_2} + 1c_{CO_2} + 1c_O + 1c_c$ $k_{f4} = \frac{1.20 \times 10^{17} [cm^3 K mol^{-2} s^{-1}]}{TC_{eff4}}$ $T_{range} = 300-3000 \text{ K}$	[49]
R5	$CO_2 + C \rightleftharpoons CO + CO$	$k_{f5} = 1.0 \times 10^{-15} [cm^3 s^{-1}] \times N_A$ $T_{range} = 300 \text{ K}$	[50]
R6	$C + O + M \rightleftharpoons CO + M$	$C_{eff6} = 1c_O + 1c_{CO} + 1c_{CO_2} + 1c_{O_2} + 1c_C$ $k_{f6} = 2.14^{-29} [cm^6 s^{-1}] \times \left(\frac{T}{300[K]}\right)^{-3.08} e^{\left(\frac{-2114[K]}{T}\right)}$ $\times N_A^2 C_{eff6}$ $T_{range} = 8000 \text{ K}$	[50]

$C_{eff}$  is the effective concentration of the third body species, which is calculated by taking the sum over the concentrations of all species  $c_i$  considered in the model, multiplied by their third-body efficiency. For the third body efficiencies, we refer to [49]. We assume that the Arrhenius fits are valid outside the optimization range, since the equation physically represents the probability that species in correct orientation will react upon collision [51].

The  $CO_2$  conversion is calculated based on the molar flow rate of  $CO_2$ , presented as most common formulation by Wanten et al. [12].

$$\chi(\%) = 100\% \times \frac{(\dot{n}_{CO_2}^{in} - \dot{n}_{CO_2}^{out})}{(\dot{n}_{CO_2}^{in})} \quad (19)$$

With  $\dot{n}_{CO_2}^{in}$  the molar flow rate (mol s<sup>-1</sup>) of CO<sub>2</sub> entering the domain and  $\dot{n}_{CO_2}^{out}$  the molar flow rate (mol s<sup>-1</sup>) of CO<sub>2</sub> exiting the fluid domain. This formula inherently accounts for gas expansion [12].

## 2.5. Heat balance equation

The heat balance equation describes the conservation of energy within the system, including the chemistry and the enthalpy transport of species: [45, 52]

$$\rho C_p \mathbf{u} \cdot \nabla T + \nabla \cdot (-(k_m + k_T) \nabla T) + \sum_i \frac{\bar{H}_i}{M_i} R_i = Q - \sum_i \mathbf{J}_i \cdot \nabla \frac{\bar{H}_i}{M_i} \quad (20)$$

With,  $C_p$  the heat capacity at constant pressure (J kg<sup>-1</sup> K<sup>-1</sup>),  $T$  the temperature (K),  $k_m$  the molecular thermal conductivity (W m<sup>-1</sup> K<sup>-1</sup>) and  $k_T$  the turbulent thermal conductivity (W m<sup>-1</sup> K<sup>-1</sup>). The molar enthalpy of species  $i$  is shown as  $\bar{H}_i$  (J mol<sup>-1</sup>),  $Q$  is the user-defined heat source (W m<sup>-3</sup>), as described in section 2.1 above. The terms on the left-hand side correspond to the convective term, the conductive term, and the term representing heat generated or absorbed by chemical reactions. The terms on the right-hand side include the heat source, mimicking the plasma, and the enthalpy diffusion. The work done by pressure and viscous dissipation are included in the model, but omitted from the equation, since they are negligible (five orders of magnitude lower compared to the user-defined heat source).

The thermophysical properties, dependent on the gas composition, are calculated as follows:

$$C_p = \sum_i \xi_i \times \frac{C_{p,i}}{M_i} \quad (21)$$

$$k_m = 0.5 \times \left( \sum_i x_i k_i + \frac{1}{\sum_i \frac{x_i}{k_{m,i}}} \right) \quad (22)$$

$$k_T = \frac{\mu_T C_p}{Pr_T} \quad (23)$$

$$\mu = \sum_{i=1}^n \frac{\mu_i}{1 + \frac{1}{x_i} \sum_{j=1, j \neq i}^n x_j \phi_{ij}} \quad (24)$$

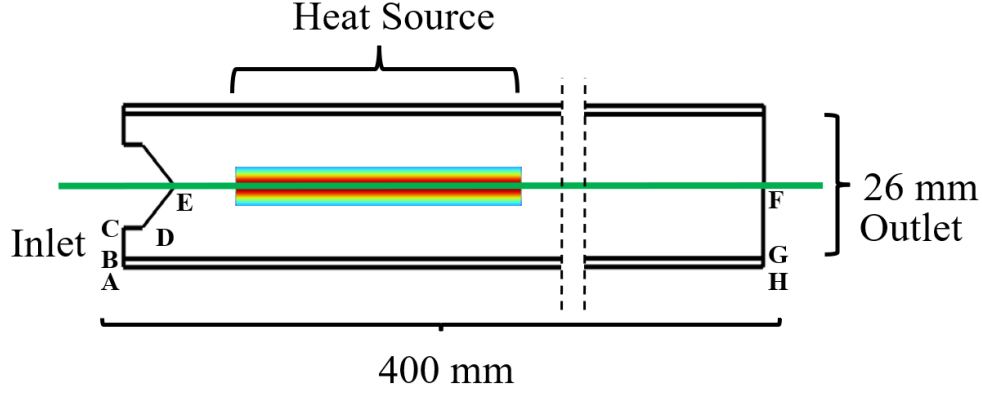
$$Pr_T = \left( \frac{1}{2Pr_{T\infty}} + \frac{0.3 C_p \mu_T}{\lambda \sqrt{Pr_{T\infty}}} - \left( \frac{0.3 C_p \mu_T}{\lambda} \right)^2 \left( 1 - e^{\left( -\frac{\lambda}{0.3 C_p \mu_T \sqrt{Pr_{T\infty}}} \right)} \right) \right)^{-1} \quad (25)$$

Here  $C_{p,i}$  refers to the heat capacity at constant pressure taken from the NASA polynomials of species  $i$  [53]. The calculation of the NASA polynomials is included in the SI (section S.5, equations 8-10).  $x_i$  represents the molar fraction of species  $i$ , and  $k_{m,i}$  is the thermal conductivity of species  $i$ . The calculation of  $k_{m,i}$  is added to the SI (section S.6, equations 11-12).  $k_T$  represents the turbulent thermal conductivity and  $Pr_T$  the Prandtl number, calculated according to the Kays-Crawford model, with  $Pr_{T\infty} = 0.85$  [48]. Finally, the calculation for the dynamic viscosity of species  $i$ ,  $\mu_i$  (Pa s) and  $\phi_{ij}$  are also added to the SI (section S.6, equations 13-15).

## 2.6. Boundary conditions of the model

The boundaries are defined as presented in Figure 1. In the 3D model, only the fluid flow boundary conditions apply, since only the gas flow is calculated. The boundary conditions for the different equations in the 2D axisymmetric model are tabulated in Table 2.

**Table 2 Boundary conditions of the 2D axisymmetric model.**



Boundary	Fluid flow	Heat transfer	Species transport
<b>AB</b> (Quartz tube)	/	$-\mathbf{n} \cdot \mathbf{q} = 0$	/
<b>BC</b> (Inlet)	$\mathbf{u} = \mathbf{u}_0$ $U_{\text{ref}} = \ \mathbf{u}_0\ $ $k = k_0$ $\omega = \omega_0$ $\nabla \cdot \mathbf{G} \cdot \mathbf{n} = 0$	$T = T_0$ ( $T_0 = 273.15 \text{ K}$ )	$\xi_i = \xi_{0,i}$
<b>CD</b> (Coaxial resonator – edge fluid domain)	$\mathbf{u} = 0$ $k = 0$ $\omega = \lim_{l_w \rightarrow 0} \frac{6\mu}{\beta_1 l_w^2}, l_w = 0$	$-\mathbf{n} \cdot \mathbf{q} = q_0$ $q_0 = h(T_{\text{amb}} - T)$ With $h = 25 \text{ W m}^{-2} \text{ K}^{-1}$	$-\mathbf{n} \cdot \mathbf{J}_i = 0$
<b>DE</b> (Coaxial resonator – edge fluid domain)	$\mathbf{u} = 0$ $k = 0$ $\omega = \lim_{l_w \rightarrow 0} \frac{6\mu}{\beta_1 l_w^2}, l_w = 0$	$-\mathbf{n} \cdot \mathbf{q} = q_0$ $q_0 = h(T_{\text{amb}} - T)$ With $h = 25 \text{ W m}^{-2} \text{ K}^{-1}$	$-\mathbf{n} \cdot \mathbf{J}_i = 0$
<b>FG</b> (Outlet)	$[-p\mathbf{I} + \mathbf{K}]\mathbf{n} = -p_0\mathbf{n}$ with $p_0 = 0 \text{ Pa}$ $\nabla \cdot \mathbf{k} \cdot \mathbf{n} = 0$ $\nabla \cdot \omega \cdot \mathbf{n} = 0$ $\nabla \cdot \mathbf{G} \cdot \mathbf{n} = 0$	$-\mathbf{n} \cdot \mathbf{q}_{\text{cond}} = 0$	$-\mathbf{n} \rho D_i^m \nabla \xi_i = 0$
<b>GH</b> (Quartz tube)	/	$-\mathbf{n} \cdot \mathbf{q} = 0$	/
<b>GB</b>	$\mathbf{u} = 0$ $k = 0$	/	$-\mathbf{n} \cdot \mathbf{J}_i = 0$

(Quartz tube – edge fluid domain)	$\omega = \lim_{l_w \rightarrow 0} \frac{6\mu}{\beta_1 l_w^2}, l_w = 0$		
HA (Quartz tube)	/	$-\mathbf{n} \cdot \mathbf{q} = \epsilon \sigma (T_{amb}^4 - T^4)$ $+ h(T_{amb} - T)$ With $h = 25 \text{ W m}^{-2} \text{ K}^{-1}$ , $\epsilon = 0.75$ and $T_{amb} = 293.15 \text{ K}$	/

With  $\mathbf{n}$  the boundary normal pointing out of the domain,  $U_{ref}$  the reference velocity scale,  $G$  the reciprocal wall distance and  $l_w$  the distance from the wall to the cell center. Furthermore,  $T_{amb}$  is the ambient temperature specified outside of the modelled domain,  $h$  the heat transfer coefficient ( $\text{W m}^{-2} \text{ K}^{-1}$ ),  $\mathbf{q}$  the total heat flux ( $\text{W m}^{-2}$ ),  $\mathbf{q}_{cond}$  ( $\text{W m}^{-2}$ ) the conductive heat flux, both defined in equation 20 in section 2.5. Furthermore  $p_0$  is the relative pressure (Pa), compared to the reference pressure defined as 1 atm, and  $\epsilon$  is the emissivity constant. The heat transfer coefficient was chosen as a representative value for the free convection of air, as suggested by Wolf et al. [15]. Lastly,  $\mathbf{K}$  is employed to abbreviate the following term from equation 5:  $(\mu + \mu_T)(\nabla \mathbf{u} + (\nabla \mathbf{u})^T) - \frac{2}{3}(\mu + \mu_T)(\nabla \cdot \mathbf{u})\mathbf{I} - \frac{2}{3}(\rho k)\mathbf{I}$ .

Note that the Stefan-Boltzmann radiation law should not include the ambient temperature. However, the simulation is not affected by this small error. Indeed, as plotted in section S.3 Figure S.5, the HA boundary quickly reaches values over 600 K. Above 600 K 95% of the radiative loss is accounted for. The formula is consequently more sensitive to the choice of the emissivity constant, as discussed in section S.3.

### 3. Results and discussion

First, in section 3.1, we validate our model by comparing the results with the experimental conversion and temperature measured by d’Isa et al. [7]. In section 3.2, we perform a sensitivity analysis on the power distribution within the model, as mentioned in section 2.1, which indicates that the chosen power distribution is not important when assessing conversion. In section 3.3, we discuss the spatial distribution of net CO production, while in section 3.4 we demonstrate that diffusion is the main driver of CO<sub>2</sub> conversion. In section 3.5 and 3.6, we present a radial reaction analysis and radial transport in the MW CO<sub>2</sub> reactor, for CO and O atoms, respectively. Last but not least, in section 3.7, we evaluate the effect of turbulence on the system, by comparing laminar and turbulent flow.

#### 3.1. Validation of the model with experiments

To validate our model against the experimental results by d’Isa et al. [7], we compare the calculated (red) and experimental (black) conversions as a function of specific energy input (SEI), as presented in Figure 3.

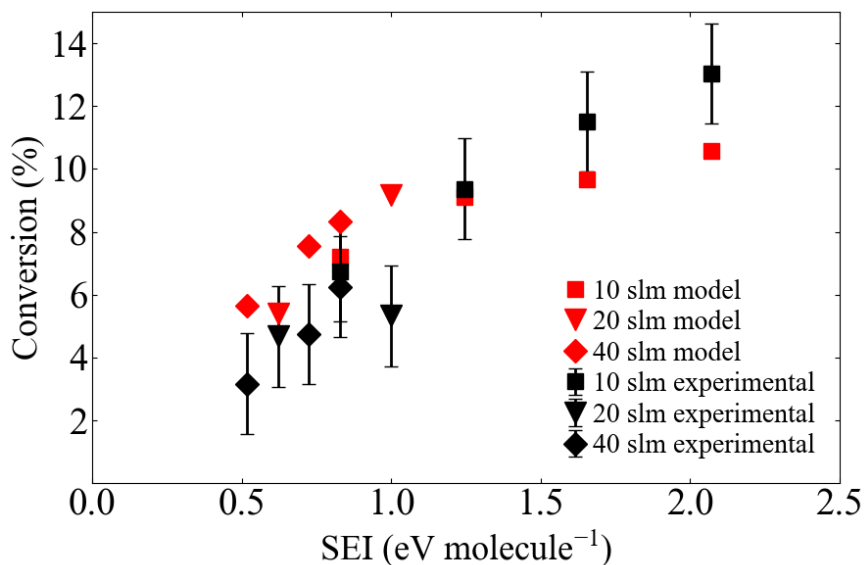


Figure 3. Calculated (red) and experimental (black) conversion as a function of SEI for different flow rates (10, 20 and 40 slm), at atmospheric pressure. The experimental data are provided by d’Isa et al. and are measured at 920 mbar (serving as a proxy for atmospheric pressure) [7].

Figure 3 demonstrates a reasonable agreement between the model and experiment, both in absolute values and trend, certainly keeping in mind that no fitting parameters are used in the model, and that, except for the power density profile, the entire model is solved self-consistently. However, at 20 slm, above 1 eV molecule<sup>-1</sup>, we observe discrepancies between experimental and calculated values. We could not yet reproduce the experimental values at higher SEI for this flow rate, due to elevated temperatures persisting until the end of the simulation domain. These high temperatures still allow for chemistry, especially recombination reactions, to take place, beyond the considered simulation domain. This makes it impossible to assess the conversion at the end of the simulation domain. Elongating the domain would lead to excessively long computation times and complications, since currently the entire length of the quartz tube (400 mm) is already modelled. Indeed, experimentally, a heat exchanger is placed after the quartz tube and modelling this heat exchanger is out the scope of our research. For the sake of information, the experimental results at higher SEI conditions are plotted in SI (section S.7, figure S.6).

The second variable that we used for model validation is the gas temperature in the plasma core. Figure 4 compares the calculated (red) and experimental plasma temperature along the radial (a) and axial (b) direction.

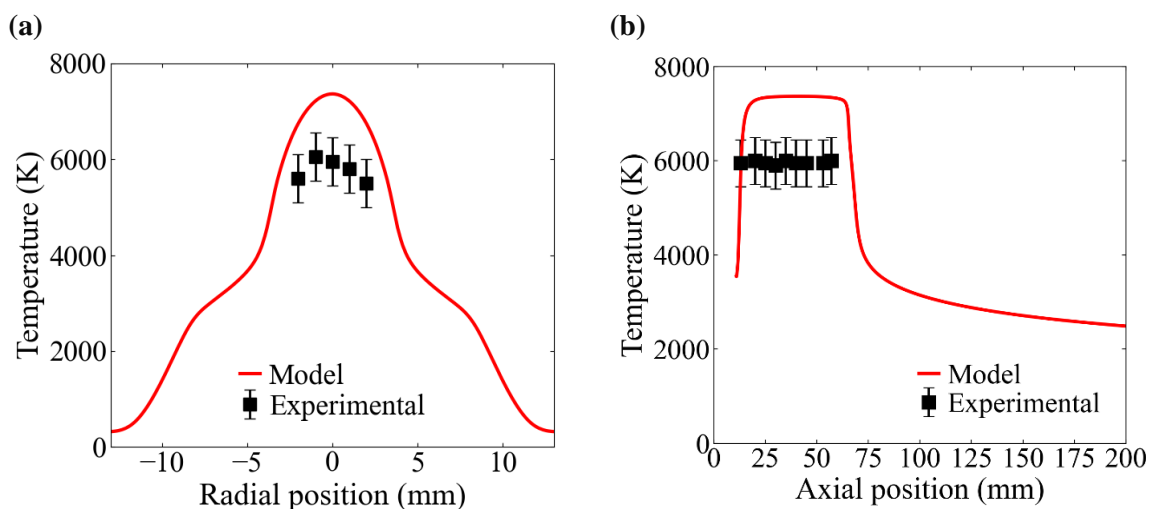


Figure 4. Comparison of the calculated (red) radial temperature profile (a) and axial temperature profile (b) at 1 atm, 900 W and 10 slm, with the experimental data (black) at 920 mbar and 10 slm, digitized from d’Isa et al. [7]. The radial temperature profile is taken at 58 mm from the bottom of the coaxial resonator (where also the experimental data were measured and indicated with an orange dotted line in Figure 1), and the axial temperature is taken along the symmetry axis of the reactor.

The calculated plasma core temperatures vary from 6660 K to 7370 K within the entire range of studied conditions (presented in Figure 3), which are higher than the measured values of around 6000 K. It is possible to match the temperature by altering the size of the heat source, however, we decided to not do this, to keep consistency with the measured plasma dimensions [7], as discussed in section 3.2. Nevertheless, the experimental trend of temperature decay along the radial direction is reflected within the limited measured range, as depicted in Figure 4 (a). This same trend is also observed in other multi-dimensional CO<sub>2</sub> plasma models [22]. We also plot the calculated temperature beyond the measured range, demonstrating that it drops quite steeply towards 300 K at the reactor walls.

Figure 4 (b) indicates that the plasma core temperature is somewhat overestimated in our model, but the temperature trend along the axial direction (i.e., constant over the entire measured distance) is well captured. The heat source for 900 W and 10 slm is located from 11 mm – 65 mm axially. The calculated temperature drops steeply beyond 60 mm, corresponding to the end of the heat source, to roughly 3500 K, and then more gradually to about 2450 K at 200 mm and 1700 K at 400 mm. D’Isa et al. did not report measured temperatures in the afterglow, and thus, the afterglow temperatures obtained by the model could not yet be validated [7]. We hope that in the future, the afterglow temperature can still be measured, to further validate the temperature profile of our model. We do not plot the temperature profile beyond 200 mm to preserve clarity. Overall, our model agrees reasonably well with the experimental results.

### 3.2. Sensitivity analysis of the heat source

As mentioned above, the power density distribution is the only parameter not calculated self-consistently within our model. Therefore, we studied the effect of a different heat source shape for a high SEI condition (1200 W and 10 slm, yielding an SEI of 1.65 eV molecule<sup>-1</sup>) and a low SEI condition (1500 W and 40 slm, SEI = 0.52 eV molecule<sup>-1</sup>), as well as some variations in the axial location of the heat source, to assess their influence on the calculated CO<sub>2</sub> conversion and plasma temperature, which were used for model validation. Varying the location of the heat source by placing it 10 mm higher or lower (cf. Figure 2) has a negligible effect on the conversion ( $\pm 0.1\%$  at SEI = 0.52 eV molecule<sup>-1</sup>). Likewise, the temperature profile moves 10 mm higher or lower along the axial direction, but with small

changes in maximum temperature ( $\pm 40$  K). At higher SEI, the effect on the temperature values becomes even less pronounced.

In addition, the shape of the heat source was taken as a rectangular function in the axial direction in first approximation, as described in section 2.1. To estimate the influence of this assumption, we modified the power distribution in the axial direction, presented in the right panel of Figure 2, to a Gaussian function. Figure 5 displays the different temperature profiles for both shapes of the heat source.

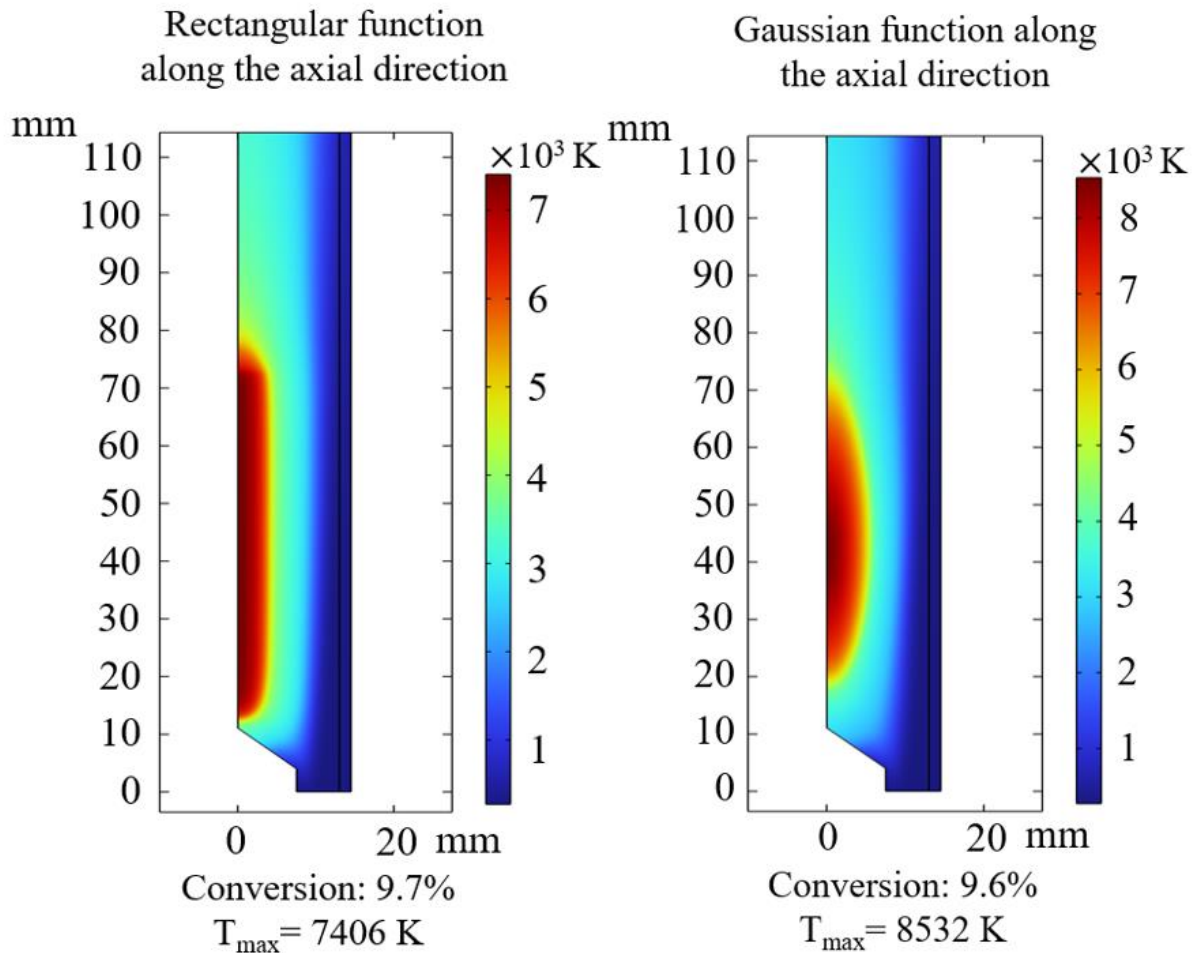


Figure 5. Different temperature profiles, for two different shapes of the heat source, i.e., a rectangular function (left) and Gaussian function (right), at 1200 W, 1 atm and 10 slm.

Varying this power density distribution affects the plasma core temperature to some extent, resulting in a difference of 1164 K at 10 slm and 1200 W (i.e.,  $\text{SEI} = 1.65 \text{ eV molecule}^{-1}$ ), while not significantly affecting the conversion, because the latter is only reduced by 0.1% at these conditions (from 9.7% to 9.6%). At lower SEI conditions, the effect on temperature becomes less pronounced, resulting in a difference of 284 K for the maximum temperature, at 40 slm and 1500 W (i.e.,  $\text{SEI} = 0.52 \text{ eV molecule}^{-1}$ ), the conversion is again only reduced by 0.1% (from 5.7% to 5.6%). Thus, the conversion is negligibly affected by changing the power distribution in our model when we adhere to the measured plasma size.

Similar methods of choosing the decay of the heat source have been used in literature. Recently, Tatar et al. measured the size and shape of the ionized region in air plasma and chose the heat source shape accordingly, resulting in a very similar shape to the rectangular function [36]. Furthermore, Kotov previously conducted a sensitivity analysis on the shape of the heat source in a 1.5D  $\text{CO}_2$  plasma model and found limited effects on conversion when altering the shape of the heat source [33].

The shape of the heat source slightly alters the temperature in the plasma core. This in turn influences the temperature gradients, which influence the transport of species, so our model is to some extent sensitive to the shape of the heat source. However, there is limited sensitivity with respect to conversion, due to how all these different physical processes interact. Figure 6 compares the temperature, net CO production rate, net volumetric source due to diffusion of CO, as well as the number density of CO, as a function of radial position along a cutline at  $z = 4.5$  cm, between a rectangular and Gaussian heat source shape. Net CO production rate is defined as the sum of the rates of all CO production reactions minus all CO destruction reactions. Note that when net CO production is negative, CO is destroyed, so we refer to negative net CO production as net CO destruction. The net diffusive transport rate is defined as the volumetric source due to diffusion, which is defined as the divergence of the diffusive flux of CO and the number density of CO is calculated based on  $\frac{N_A \cdot \xi_{CO} \cdot \rho}{M_{CO}}$ . The cutline of  $z = 4.5$  cm was chosen, since the core temperature difference between the rectangular and Gaussian heat source shape is the largest at this cutline.

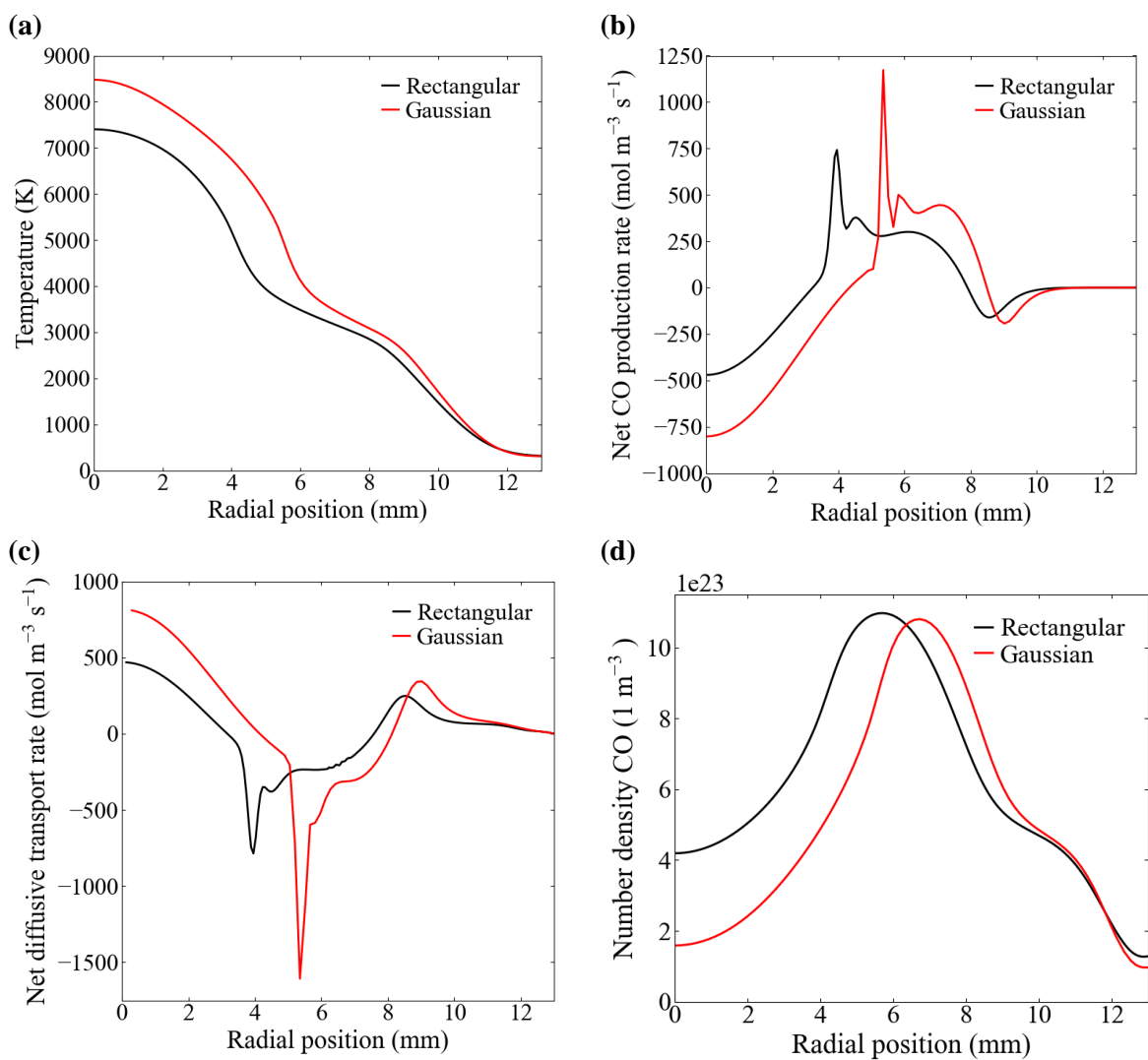


Figure 6. Comparison of temperature, net CO production rate, net diffusive transport rate of CO, and CO number density between the Gaussian and rectangular heat source shape, as a function of radial position, on a cutline of  $z = 4.5$  cm for 1200 W and 10 slm.

As can be seen from Figure 6 (a), the absolute values of temperature are somewhat sensitive to the shape of the heat source, as more power is deposited in a smaller region for a Gaussian shape (red) compared to a rectangular shape (black), while the temperature decay shows similar profiles. This change in temperature leads to changes in the reaction rates and consequently in the transport of species. Figure 6 (b) shows that when a Gaussian profile is employed (red), the net CO production rate is clearly higher around  $r = 5$  mm compared to the rectangular shape. The strong increase in net CO production rate at around 5 mm leads to more CO diffusion out of this region, as can be seen from Figure 6 (c). Most of this CO diffuses to the center of the reactor ( $r < 4$  mm), whereas net transport to the edge of the domain ( $r > 7$  mm) is almost identical. As can be seen from Figure 6 (d), the number density of CO is clearly lower in the center of the plasma for a Gaussian heat source shape (red). The CO that is produced at the edge of the plasma (around 5 mm) diffuses to the center of the reactor. As can be seen from Figure 6 (b), with a Gaussian shape (red) the net CO destruction rate (defined as negative net CO production rate) in the center is clearly higher. At the edge of the reactor ( $>10$  mm), the number density of CO is nearly identical. This is the region where CO can be convectively transported outward. Indeed, as can be seen from Figure 6 (b), at the edge ( $>10$  mm) no CO is produced nor destroyed. The net reaction rates and net transport rates are extensively analysed in sections 3.6 - 3.8 below. In conclusion, in the entire domain, both the net CO production rate ( $5 \text{ mm} < r < 8 \text{ mm}$ ) as well as the net CO destruction rate ( $r < 4 \text{ mm}$ ) are stimulated locally, when using a Gaussian heat source shape compared to a rectangular one. However, as there is similar net transport to the edge of the reactor ( $r > 10 \text{ mm}$ ) for both heat source shapes, this results in nearly identical conversion.

Most importantly, the temperature profile, net CO production rate profile and net diffusive transport rate profile are very similar when comparing both heat source shapes (so mainly their absolute values differ). This shows that even for small deviations in the heat source shape compared to reality, our model can effectively capture the phenomena that play an important role in determining both the temperature and conversion effectively. Furthermore, it shows that conclusions drawn from our model using the rectangular heat source shape, in terms of the importance of diffusion and where CO is produced, are valid, even in case of deviations in the shape of the heat source.

It needs to be noted that the deviation in heat source shape considered here is limited, since we adhere to the measured plasma dimensions. Viegas et al. reported that optical contraction, at pressures below 150 mbar, might cause an underestimation in the width of the heat source by a factor of 1.6 [54]. The effect is not reported at higher pressure, but was considered in the SI, section S.8, for the sake of completeness. Furthermore, it is known that SST models are sensitive to boundary conditions for both the specific dissipation rate and the turbulent kinetic energy, and the influence of both parameters at the inlet is discussed in the SI, section S.9 [55].

We decided to apply the rectangular function along the axial direction, for all conditions investigated, since this function aligns best with the temperature profiles measured by d'Isa et al., while adhering to their measured plasma dimensions and total deposited power [7].

### 3.3. Where does the CO<sub>2</sub> conversion happen in the plasma reactor?

Several recent studies suggested that the CO<sub>2</sub> conversion in plasmas may occur solely at the plasma edges [20, 22, 23, 33]. Most recently, Kotov et al. predicted that the radial diffusion of both CO and O atoms drives conversion in CO<sub>2</sub> plasma, based on their 1.5 D model [33]. To verify whether indeed the CO<sub>2</sub> conversion occurs in the plasma edges, and to explain the underlying reason, we plot in Figure 7 the temperature profile within the reactor (left) and the net CO production rate (right), for 1500 W, 1 atm and 10 slm. The net CO production rate is defined as the sum over the net rates of all CO production reactions minus all CO destruction reactions.

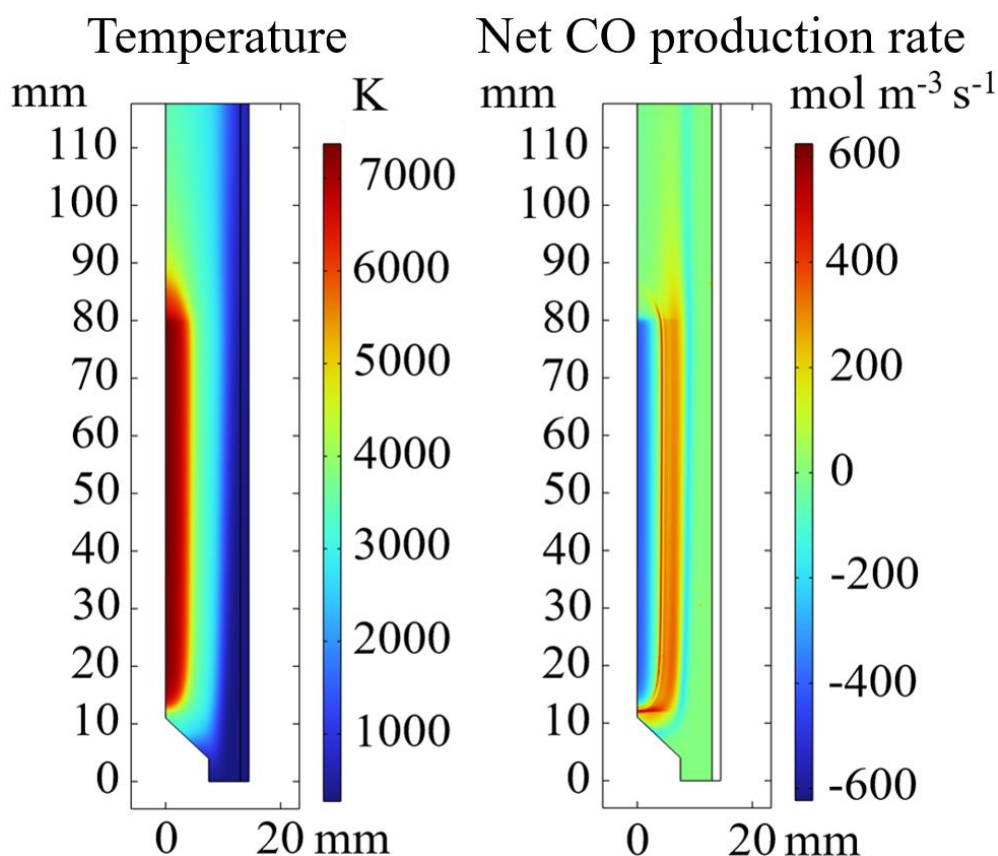


Figure 7. Temperature profile (left) and net CO production rate profile (right) for 1500 W, 1 atm and 10 slm.

As can be seen in Figure 7, there is only net CO destruction in the center of the plasma. The majority of net CO production occurs at the plasma edges of the MW reactor, where significant chemical non-equilibrium occurs. Van Alphen et al. previously calculated the fluid velocity and temperature profile, based on the assumption of LTE for the same plasma reactor, using these profiles as input for a 1D chemical kinetics model (only taking convection into account), and they found that the production and destruction rates are balanced in the plasma when temperatures exceed 4000 K [22]. However, due to diffusion of C atoms in the radial direction, we observe net CO production at temperatures around 5000-5500 K and net destruction in the plasma core. Hence, temperature is not the only important factor determining net CO production, but net species transport is also very important; it causes the net rates to be non-zero in the plasma, as can be seen in Figure 7, as well as in the Supplementary Information section S.10. Kotov et al. previously plotted the net CO<sub>2</sub> source, as well as the CO<sub>2</sub> sink, and found similar profiles in their model, for this reactor, whilst not accounting for the swirl flow [33]. A detailed spatial analysis of the net reaction rates and net transport rates for these conditions (10 slm and 1200 W, corresponding to an SEI of 1.65 eV molecule<sup>-1</sup>) will be given below.

### 3.4. Diffusion is the main driver of conversion in MW CO<sub>2</sub> plasmas.

Murphy et al. indicated that the LTE approximation is not sufficient to determine the local composition in plasmas with multiple chemical elements [56]. The concentrations of chemical species vary non-uniformly across the plasma due to differences in diffusion velocities among species in MW CO<sub>2</sub> plasmas. Nevertheless, CO<sub>2</sub> plasmas are often assumed to be in LTE (e.g., spectroscopic measurements based on LTE assumption, and chemistry calculations for LTE conditions) [15, 22, 23, 57]. A more detailed discussion on why the LTE assumption is not valid is added in the SI, section S.10.

Species transport is determined by both diffusion and convection (cf. equation 8 above). We can estimate the influence of diffusion on the conversion by running our model, only ignoring molecular and turbulent diffusion, while still considering convective transport of species. Molecular diffusion is ignored by reducing the molecular diffusion constants to 1% of their original value, turbulent diffusion is ignored by setting the Turbulent Schmidt number to 400 (cf. equation 17), and consequently, the diffusive flux is reduced below 1% of its original value. Further lowering of both the molecular and turbulent diffusion led to computational instabilities.

Figure 8 displays the difference in calculated conversion for the model where all physics considered are fully coupled (FC; black) and when diffusion is neglected (ND; red), using the same temperature and velocity profiles.

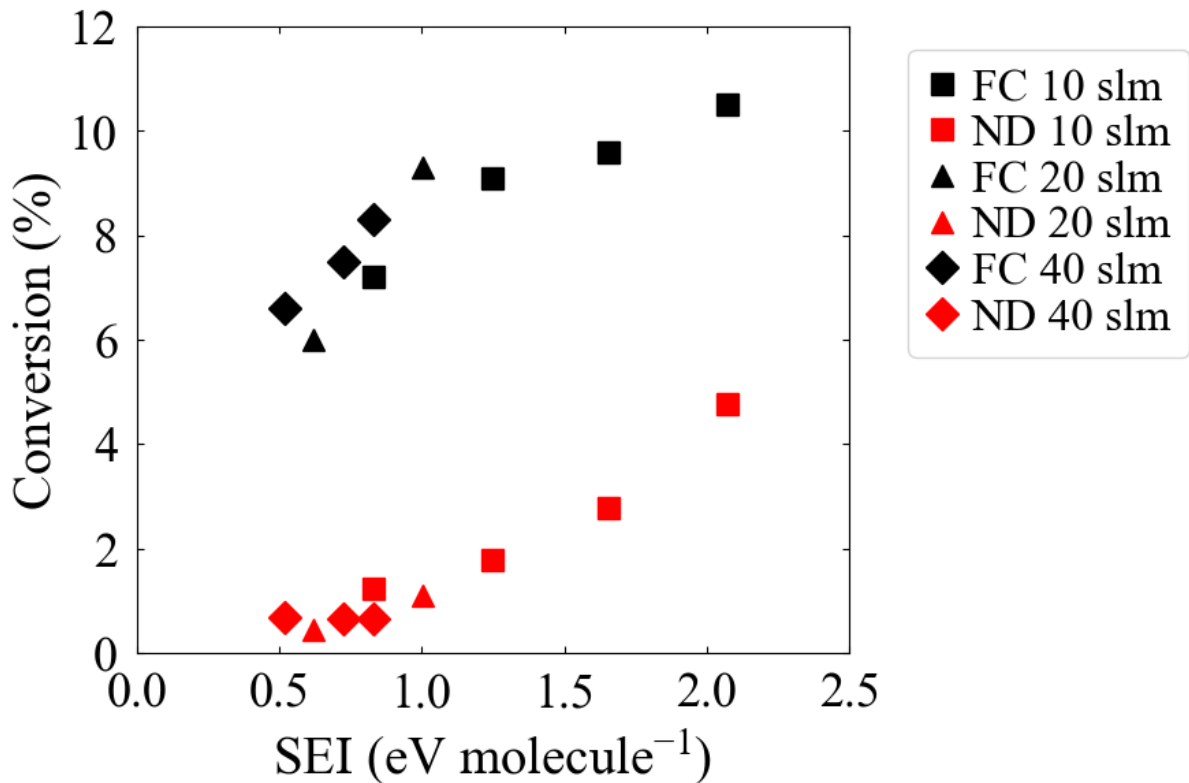


Figure 8 Comparison between the calculated CO<sub>2</sub> conversion for the model where all physics considered are fully coupled (FC; black) and when neglecting diffusion (ND; red), the red values should be judged relatively to the black data points.

As can be seen from the large difference between black and red data points in Figure 8, diffusion is undoubtedly the main driver for conversion in MW CO<sub>2</sub> plasmas. The computations where diffusion is neglected are representative for the fraction of CO<sub>2</sub> conversion driven by convective transport in the model where all physics considered are coupled.

In other words, the fraction of conversion driven by convective transport is much lower than the fraction driven by diffusion. The importance of diffusion indicates the importance of solving models in higher dimensions, rather than 1D. Kotov et al. previously indicated the need for higher dimensional modelling of CO<sub>2</sub> microwave plasmas [33].

As previously discussed, net CO production occurs predominantly at the plasma edges. Therefore, when diffusion is not considered, at identical flow rates, the conversion increases with increasing SEI, due to the radial expansion of the plasma, which is dependent on the input power (plotted in the SI, section S1, Figure S1a). Indeed, a larger fraction of the gas is treated when the plasma expands radially. Note that when diffusion is considered, particles migrate back and forth between the cold edge and the hot plasma core.

Intuitively, convective transport is expected to account for a larger fraction of conversion at higher flow velocities. The cooling rate is calculated based on the substantial derivative along the axial direction, which represents the rate of change in temperature which species experience when moving with the gas flow along the axial direction. The cooling rate is in the order of  $10^4$ - $10^5$  K s<sup>-1</sup> in the afterglow, except right after the heat source, where values of  $10^6$  K s<sup>-1</sup> are reached, for all calculated conditions. After the steep temperature drop right after the plasma, temperatures are still sufficiently high to sustain chemical reactions. Increasing the flow rate does not increase the cooling rate substantially enough to increase quenching. Furthermore, when diffusion is not considered at higher flow rates, a higher fraction of the gas stays at the edge of the reactor, resulting in less gas passing through the hot zone, resulting in lower conversion compared to lower flow rates, when diffusion is not considered.

In conclusion, diffusion is fast enough to disrupt chemical equilibrium in the MW CO<sub>2</sub> plasma, locally altering the concentration of reagents and consequently influencing the reaction rates. Radial diffusion leads to retention of the formed CO, as will be discussed in detail in sections 3.5 and 3.6. We will perform a spatial reaction analysis in the radial direction for both CO and O (in sections 3.5 and 3.6, respectively) for the thermo-chemical model, presenting their net production rates, based on all reactions considered in the model, which will provide detailed insight into the mechanisms driving CO<sub>2</sub> conversion. Furthermore, the effects of turbulent diffusion and turbulent heat transfer on the conversion and temperature profile will be discussed in section 3.7.

### 3.5. Radial reaction analysis and radial transport of CO molecules

Figure 9 presents the different components governing conservation of mass (cf. equation 8) of CO at steady state, i.e., the net reaction rates, the net diffusive transport rate, and the net convective transport rate of CO, as a function of radial position, for an axial position of 55 mm (i.e., the plasma center). Note that the net rates do not provide information about the importance of the individual (forward or backward) reactions, i.e., when both forward and backward reaction rates are very large, the net rate will be small. Nevertheless, the net rate is most important as it determines the net production or destruction of species. Hence, Figure 10 provides information not only about net spatial transport, but also about which reaction is the dominant driver for either net CO production or destruction at that position. The sign of the transport is chosen so that positive values indicate transport into that region, whereas negative values indicate transport out of that region. The sign of the reaction rates is chosen so that positive rates correspond to net CO production, and negative rates correspond to net CO destruction.

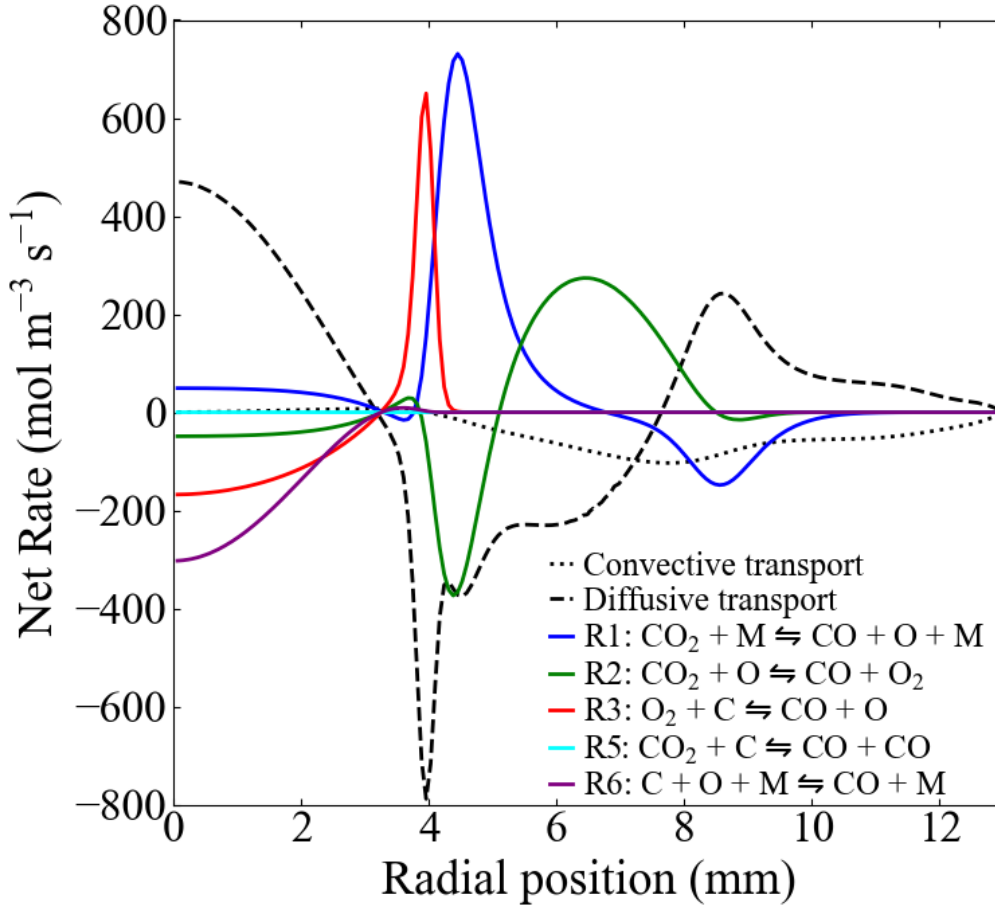


Figure 9. Calculated net reaction rates of reactions involving CO, as well as the net convective and diffusive transport rates, as a function of radial position, at an axial position of 55 mm, for 10 slm, 1200W (corresponding to an SEI of  $1.65 \text{ eV molecule}^{-1}$ ) and 1 atm. The sign of the reaction rates is chosen so that positive values correspond to net CO production, and a positive sign for the transport corresponds to CO being transported into that region.

As can be seen from Figure 9, the rates follow a ‘wave’ like pattern, driven by the variation in temperature, as well as the variation in the concentration of species participating in the reactions locally. A similar dependence was observed by Maerivoet et al. for the oxidative  $\text{CO}_2$  reforming of methane [58].

In the plasma core, with a radial position up to 3 mm, CO is provided almost exclusively by radial diffusion from the plasma edge (i.e., radial position 3-8 mm), as is apparent from the high values of net diffusive transport in this region (black dashed line). There is also net convective transport in this region, but the net convective transport of CO is negligible, to ensure conservation of mass, since there is a negligible CO concentration gradient (cf. equation 8) in the z-direction at 55 mm (i.e., the plasma center) and the r-velocity of the gas becomes negligible in the plasma core (cf. equation 8).

The temperature in the plasma core is so high (cf. Figure 4) that CO is dissociated into C and O or  $\text{O}_2$ , by the backward reactions of R6 and R3 respectively, with R6 being the main driver for CO dissociation. Reaction R2 also proceeds in the backward direction, resulting in net  $\text{CO}_2$  production in the plasma core, which reacts away immediately by R1, at steady state. In the plasma core, the C atoms are exclusively formed by the backward reactions of R3 and R6. The formed C atoms diffuse very fast along the r-direction (up to  $72 \text{ m s}^{-1}$ ), and at 4 mm (where temperatures between 5000-5500 K are reached), they react back with  $\text{O}_2$  by R3, producing again CO (and O atoms) in the plasma edge (see Figure 10). However, since all C atoms are created by dissociation of CO (by means of backward R3

and R6), diffusion of C atoms can only cause additional conversion upon reacting with CO<sub>2</sub> according to R5, which does not occur.

Once the temperature has sufficiently dropped, i.e., around a radial position of 4.5 mm, reaction R1 (i.e., the direct dissociation of CO<sub>2</sub>) becomes the dominant driver for net CO production, but is partially balanced by the backward reaction of R2. However, from a radial position of ca. 5 mm, R2 also starts to contribute to net CO production, hence it proceeds in the forward direction. Between ca. 3 and 7.5 mm, there is net CO production (cf. also Figure 7 (b) above), which diffuses largely to the plasma center and in part to the reactor edge (cf. dashed line in Figure 10), where it recombines with O atoms, mainly by the backward reaction of R1, effectively forming CO<sub>2</sub> again. However, not all CO can recombine with O atoms, as will be explained in more detail in section 3.6.

A small part of the formed CO diffuses further into the cold gas stream at the edge of the reactor (beyond a radial position of 10 mm), where the chemistry is frozen. In contrast, all net convective transport happens to the center (symmetry axis) since the velocity in the r-component is exclusively negative. Therefore, some of the CO that diffuses to the cold gas stream will be transported along the z-direction and back into the plasma edge by convection. To illustrate this, we plot the entire gas velocity profile and the different velocity components in SI (section S.11, figure S.16 and S.17, respectively). At the edge of the reactor, i.e., at a radial position of 8-12 mm, the net transport towards the center by convection is balanced by the net diffusive transport towards the edge (cf. Figure 10). The balance between the inward net convective transport and outward net diffusive transport makes that the cold gas at the reactor edge at this axial position contains low molar fractions (2-3%) of CO (cf. Figure 8 above).

In conclusion, our analysis reveals that net CO production occurs mainly at a radial position of 3-6 mm, and that most of it diffuses radially toward the plasma core, where it is dissociated due to the high temperatures. The fraction of CO that is effectively recovered, and which is the driver of the CO<sub>2</sub> conversion, is produced in the lower temperature region, at a radial position of ca. 6-8 mm, upon reaction of CO<sub>2</sub> + O (R2). In the outer region, beyond 10 mm, net diffusion outward is balanced by net convective transport inward due to the swirling flow. The CO present in the outer gas stream is then transported axially with the gas flow to the reactor outlet.

### 3.6. Radial reaction analysis and radial transport of O atoms

It is clear from section 3.5 that the conversion of CO<sub>2</sub> is driven by reactions involving O atoms, and thus, we also need to understand their net production rates and net radial transport rates. Figure 10 displays the different components governing the conservation of mass of the O atoms at steady state, i.e., their net reaction rates, their net diffusive transport and net convective transport, as a function of radial position, for an axial position of 55 mm (i.e., the plasma center). The sign of the transport is chosen so that positive values indicate net transport into that region, whereas negative values indicate net transport out of that region. The sign of the reaction rates is chosen so that positive rates correspond to net O production, and negative rates correspond to net O destruction.

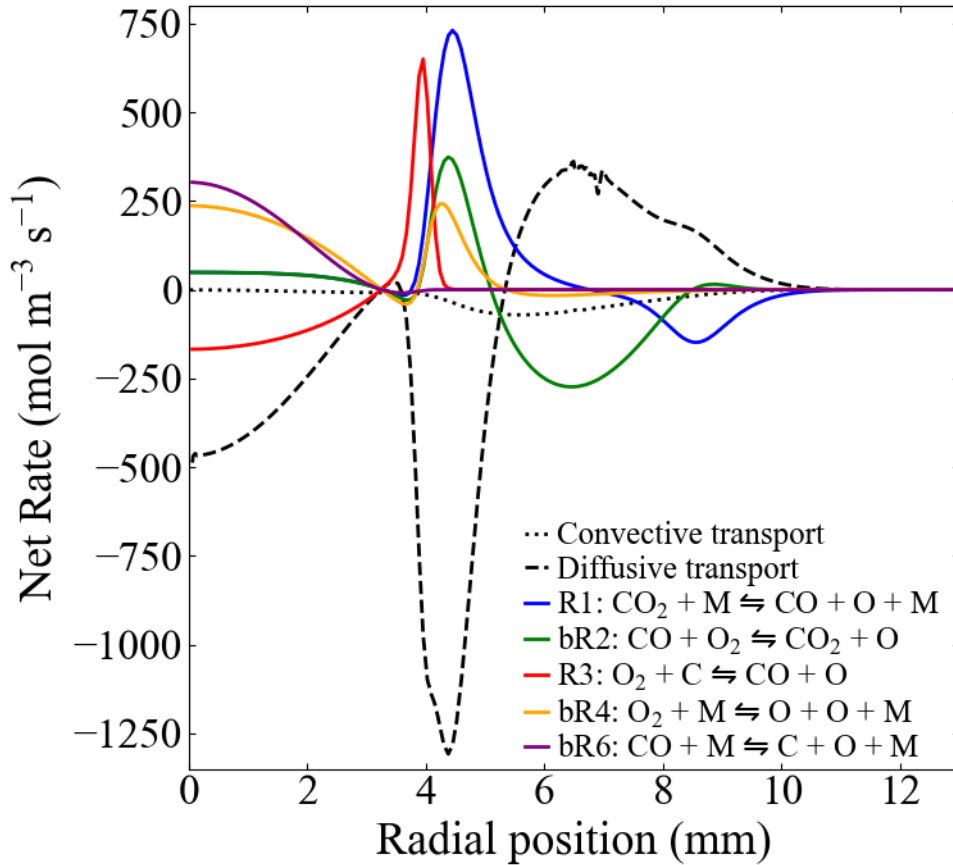


Figure 10 Calculated net reaction rates of reactions involving O atoms, as well as the net convective and diffusive transport rates, as a function of radial position, at an axial position of 55 mm, for 10 slm, 1200 W and 1 atm. The sign of the reaction rates is chosen so that positive values correspond to net O atom production, while a positive sign for the transport corresponds to O atoms being transported into that region. Note that R2, R4 and R6 are written in the backward direction in the legend, as compared to Table 1, hence the notation “b”.

Net O atom production occurs in the entire plasma and at the plasma edge. In the center of the plasma, the backward reactions of R6 and R4 (i.e., direct dissociation of CO and O<sub>2</sub>) are the main drivers for net O atom production. O<sub>2</sub> in the center of the plasma is produced by the backward reaction of R3, but instantly decomposes according to the backward reaction of R4, so that the molar fraction of O<sub>2</sub> is negligible inside the plasma. R3 and R4+R2 are not completely balanced, indicating that the additional O<sub>2</sub> is provided by net diffusion towards the center.

The O atoms produced in the center diffuse towards the plasma edge (see dashed line in Figure 10), where more O atoms are produced, primarily by R3 and R1. In this region, the temperature is still high enough to dissociate O<sub>2</sub> directly, yet most O<sub>2</sub> will recombine with CO, to form CO<sub>2</sub> and O atoms, by the backward reaction of R2. The O atoms produced in this region diffuse further to the edge of the reactor (see dashed line), leading to additional net CO production when the O atoms collide with CO<sub>2</sub>, by R2.

Note that Kotov et al. reported, based on 0D calculations, that most O atoms recombine to O<sub>2</sub> [33], but our model reveals that the direct recombination of O to O<sub>2</sub> by R4 is of minor importance. Instead, the O atoms that diffuse towards the reactor edges react with CO<sub>2</sub> according to R2, until about  $r = 8.5$  mm. At larger radial distances, R2 becomes negligible because of too low temperature at the edge of the reactor. We can consider a small portion of the O atoms “trapped” in O<sub>2</sub>, which is not reactive anymore at  $r = 9.5$  mm. Consequently, when all remaining O atoms recombine with CO into CO<sub>2</sub> by the backward reaction R1 in the region  $r = 7-10$  mm, not all CO has been destroyed, allowing a portion of CO to diffuse into the cold gas stream, as explained in previous section.

In earlier work, Bongers et al. hypothesized that radial diffusion of O atoms improves the CO<sub>2</sub> conversion by stimulating R2, and that otherwise the O atoms diffuse further towards the reactor edges, where they recombine into O<sub>2</sub> through R4 [57]. Similarly, den Harder et al. also suggested that the O atoms radially diffuse out of the plasma center and reach the cold CO<sub>2</sub> stream at the reactor edges, where they form additional CO [18]. However, our study reveals that the radial diffusion of O atoms contributes to CO<sub>2</sub> conversion closer to the plasma (i.e., at a radial position of 5 - 8 mm) instead of at the reactor edges, by the reaction of O + CO<sub>2</sub> (R2), whereas at  $r = 8 - 10$  mm, they recombine with CO that diffuse to the reactor edges, forming CO<sub>2</sub> again (i.e., backward reaction of R1). The CO molecules that recombine with O atoms at  $r = 8.5$  mm would otherwise be transported to the outlet by convection at the reactor edges. In other words, according to our model, there is net diffusive transport of O atoms radially out of the plasma center, contribute to more CO<sub>2</sub> conversion by reacting with CO<sub>2</sub> molecules (producing more CO) at radial positions between 5 and 8 mm, but in addition, they also recombine with CO into CO<sub>2</sub> again, further near the reactor edges, between  $r = 8$  and 10 mm, thus reducing the net CO<sub>2</sub> conversion.

In literature, several authors proposed R4 as the dominant recombination reaction for O atoms, based on 0D calculations or a more qualitative assessment of the reactions [7, 33, 57]. However, our model predicts that R4, i.e., recombination of O atoms into O<sub>2</sub>, is negligible at plasma height, and recombination of O atoms with CO (via the backward reaction of R1) is dominant. This insight can only be obtained from a 2D thermo-chemical model which properly accounts for transport of species.

In conclusion, net radial diffusion of O atoms is almost exclusively to the edge of the reactor. Radially diffused O atoms that react with CO<sub>2</sub> according to R2 lead to O being ‘trapped’ in O<sub>2</sub> and additional net CO production in a temperature region where O<sub>2</sub> is stable. This allows radially diffusing CO molecules to reach the cold gas stream at the edge of the reactor, without recombining with O to CO<sub>2</sub> according to R1.

### 3.7. Importance of turbulence in the CO<sub>2</sub> MW plasma

#### 3.7.1 Turbulence increases with higher flows

To the best of our knowledge, the effects of turbulence in a CO<sub>2</sub> MW plasma reactor have not been investigated in detail. Therefore, in what follows, we present exclusively theoretical results that have not been experimentally validated yet. As previously stated in the introduction, not all multi-dimensional models account for turbulence [5, 15, 26]. The turbulent intensity is used to gauge whether a flow is turbulent and is defined as [59]:

$$I_{Turb} = \frac{\sqrt{\frac{2}{3}k}}{U_{ref}} \quad (\text{Eq. 26})$$

With  $U_{ref}$  the reference velocity, defined as the maximum velocity magnitude (equal to 5.9 m s<sup>-1</sup> for 10 slm and 12.9 m s<sup>-1</sup> for 40 slm at 1500 W). Figure 11 shows the relative turbulent intensity for 10 slm and 40 slm, at 1500 W and 1 atm.

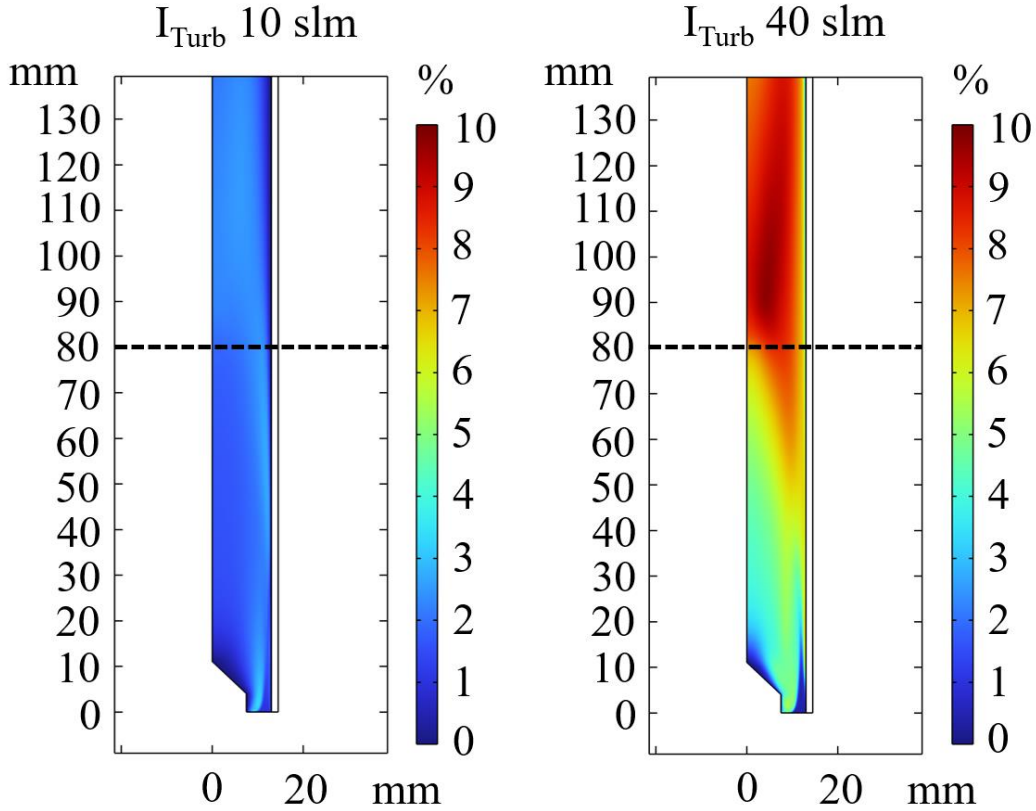


Figure 11. Relative turbulent intensity comparison between 10 slm (left) and 40 slm (right) at 1500W and 1 atm. The end of the heat source is indicated by the black dashed line.

As can be seen in the figure, the relative turbulent intensity is considerably smaller at lower flow rates (10 slm) compared to higher flow rates (40 slm). At higher flow rates, the relative turbulent intensity increases drastically, especially after the plasma. The sharp rise in relative turbulent intensity and consequently in turbulent kinetic energy at the end of the heat source (representing the plasma; (indicated with a black dashed line)) can have a strong influence on the temperature profile in plasma reactors. Alternatively, we can estimate the importance of diffusion by plotting the ratio of turbulent

net diffusive flux of CO<sub>2</sub> over the total net diffusive flux of CO<sub>2</sub> (i.e. the sum of net turbulent diffusive flux and net molecular diffusive flux), as presented in % in Figure 12.

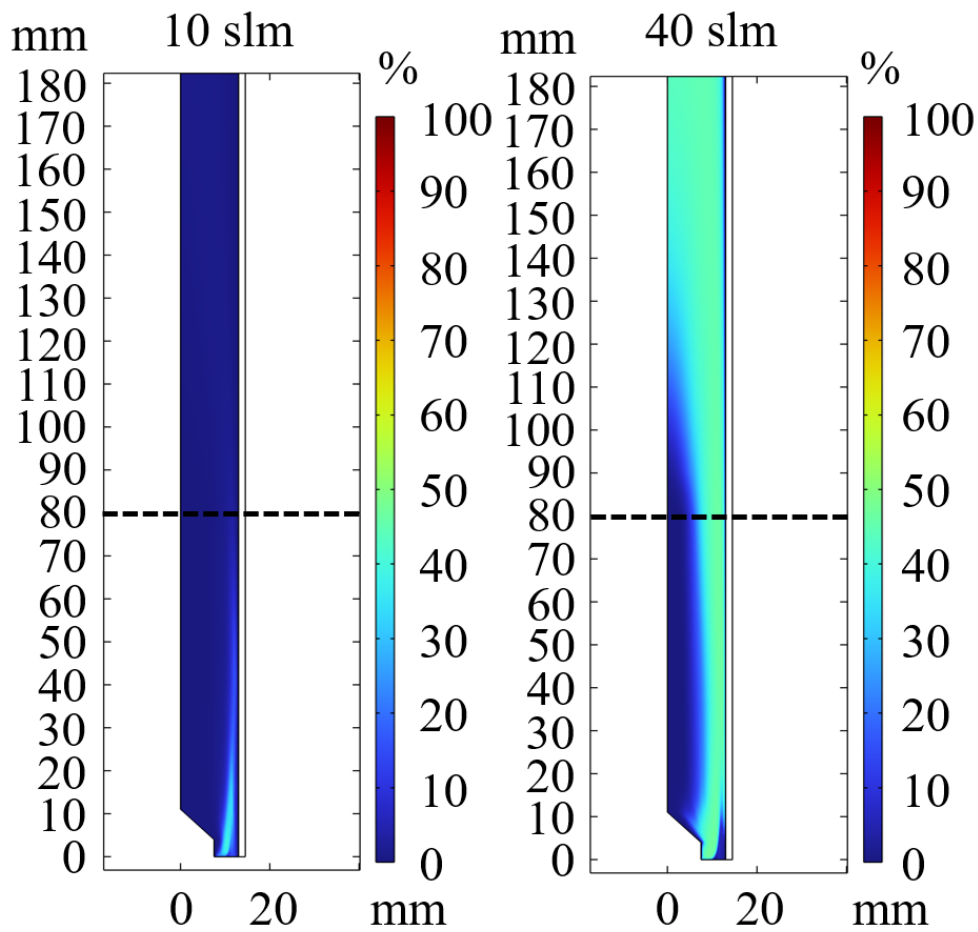


Figure 12. Relative importance of turbulent diffusion compared to the total diffusion of CO<sub>2</sub>, expressed in % as a percentage, for 10 slm (left) and 40 slm (right), both at 1500 W. The end of the heat source is indicated by the black dashed line.

As can be seen in Figure 12, at lower flow rates (10 slm) and thus higher SEI (2.07 eV molecule<sup>-1</sup>), turbulent diffusion of CO<sub>2</sub> becomes clearly less important than at higher flow rates (40 slm) and thus low SEI (0.52 eV molecule<sup>-1</sup>). Moreover, even at 40 slm, turbulent diffusion becomes negligible compared to molecular diffusion in the hot plasma zone, since the kinematic viscosity increases with temperature. This reduces the amount of turbulence in the hot region of the plasma reactor.

### 3.7.2 Effect of turbulence on the temperature profile in the reactor

Wang et al. accounted for the heat dissipation by turbulence by artificially extracting heat out of the reactor, and in this way their model was able to reproduce the measured temperature profiles quite well [5]. We now estimate the effect of turbulent mixing on the temperature within the plasma, as well as in the afterglow, by comparing laminar flow, defined here by numerically neglecting turbulent heat transfer and turbulent diffusion, while taking the turbulent viscosity in the momentum equation into account on the mesh described in section S.2.2, with the SST turbulence model. The turbulent heat transfer and turbulent diffusion are neglected, by defining the Schmidt number and the Prandtl number as  $10^5$ , effectively making the turbulent diffusion coefficient (cf. equation 17) and the turbulent thermal conductivity (cf. equation 23) negligible.

Figure 13 compares the temperature profile along the symmetry axis, calculated for laminar and turbulent flow, for 10 and 40 slm, both at 1 atm and 1500 W. The turbulent intensity is plotted in Figure 11, for both 10 slm and 40 slm, indicating that the turbulent heat transfer and turbulent diffusion will be most notable at higher flow rates.

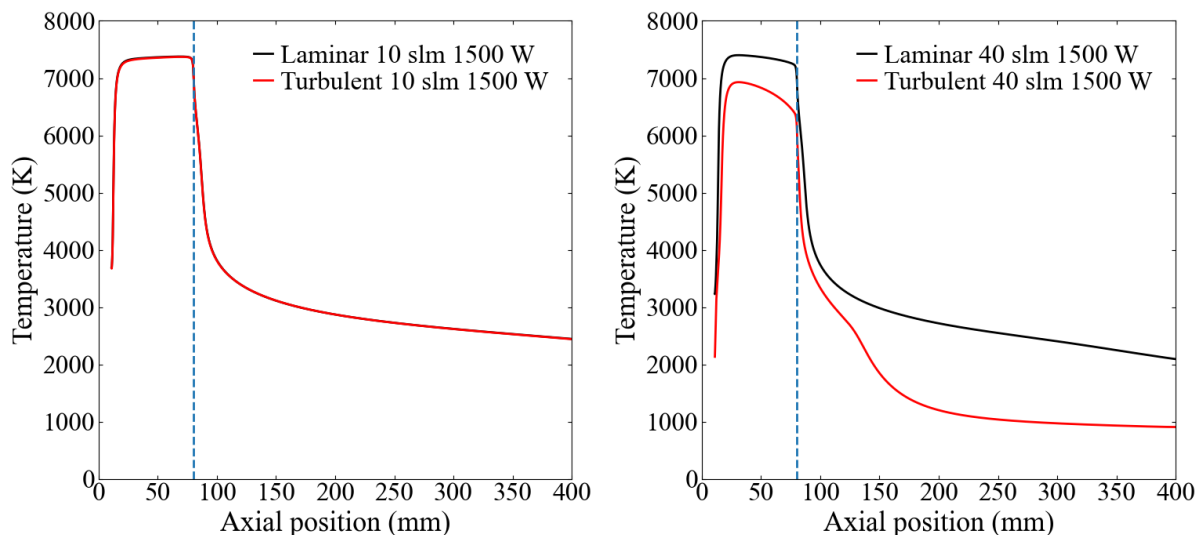


Figure 13. Comparison of temperature profile along the symmetry axis for laminar (black) and turbulent (SST; red) flows, at 1 atm, 1500 W, 10 slm (left) and 40 slm (right). The end of the heat source, and thus the start of the afterglow, is indicated by the vertical dashed line (blue).

As can be seen in Figure 13, the temperature only changes negligibly for the lower turbulence case (10 slm), while it changes notably at higher turbulence (40 slm), for the same 1500 W heat source defined in the SI, section S.1. We can see that the addition of turbulence increases the cooling rate in the afterglow (i.e., beyond the blue vertical dashed line) at higher flow rates. The drop in both core plasma temperature and afterglow temperature plasma, indicate that turbulence can be important for calculating temperature profiles in  $\text{CO}_2$  MW plasmas at higher flow velocities. The difference between the temperature profiles in the afterglow is a direct consequence of the heat transfer due to turbulence, which results from the increased turbulent thermal conductivity as well as the difference in the heat of reactions due to turbulent diffusion and the altered temperature profile. Since the relative turbulent intensity at plasma height is highest at the edge of the fluid domain, a larger increase in turbulent heat transfer is expected at the edge of the fluid domain at plasma height. The r-component of the molecular thermal conductivity and of the turbulent thermal conductivity are plotted in Figure 14.

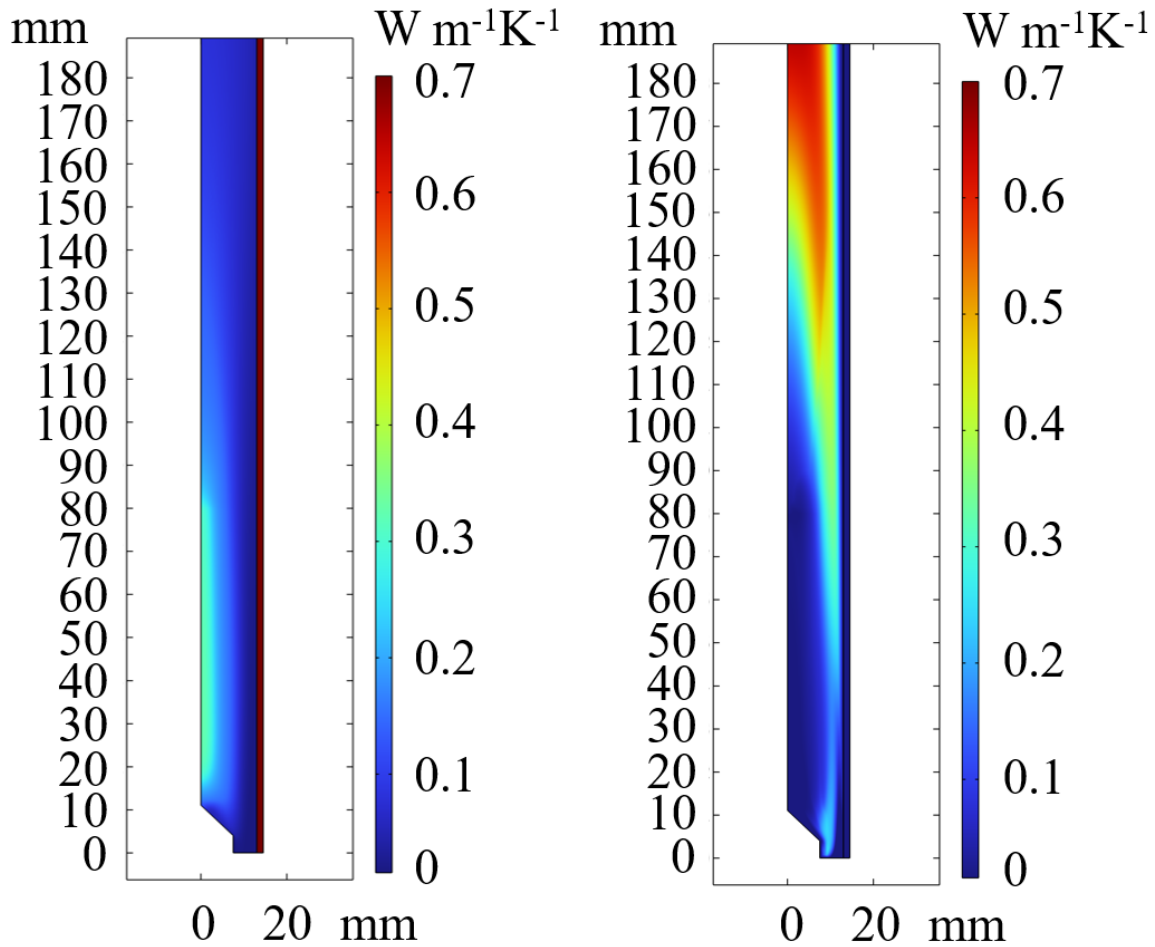


Figure 14 r-component of the effective mean molecular thermal conductivity (left) and of the turbulent thermal conductivity (right), at 40 slm, 1 atm and 1500 W, solved with the SST turbulence model.

As can be seen from Figure 14 (right), the turbulent thermal conductivity is small in the center of the quartz tube at plasma height, and becomes significant at the edge of the fluid domain, effectively increasing the total thermal conductivity of the fluid by an order of magnitude in this region. The increased thermal conductivity, especially at the edge of the fluid domain, allows for significantly faster heat transport out of the plasma core towards the edges of the fluid domain. This is the main route for heat dissipation out of the modelled domain. The net outflow of energy through the quartz tube for the laminar flow at 40 slm and 1500 W is equal to 40 W, whereas for SST turbulent flow under the same conditions, the net outflow of energy through the quartz wall is 240 W, while the residual heat of the mixture is dissipated through the outlet. Hence, under these conditions, roughly 16% of the energy supplied to the plasma is dissipated through the wall of the quartz tube. Therefore, not accounting for turbulent heat transfer may lead to an overestimation of the gas temperature in the afterglow, as observed in literature [5, 27].

After the plasma, the turbulent thermal conductivity becomes important in the center of the quartz tube as well. We hope that in the future, the afterglow temperature can still be measured, to validate the impact of the turbulent heat flux on the temperature profile.

### 3.7.3 Effect of turbulence on species transport

Turbulent effects are a direct consequence of the gas flow field in the reactor, highlighting the need for coupled solutions of the plasma behavior and gas fluid dynamics when modelling plasma reactors, especially at higher flow rates. Firstly, as presented in Table 3, we compare the measured conversion with the conversion calculated from our laminar model, defined in section 3.7.2, and the conversion calculated from our turbulent model, in both simulations all physics considered in the model are coupled, the laminar model only neglects turbulent heat transfer and turbulent diffusion.

**Table 3. Comparison between the experimental and calculated conversions, both neglecting turbulent heat transfer and turbulent diffusion (named laminar), and by a thermo-chemical model considering turbulence. The calculated values that are within error of the experiment are indicated in green, while the black values are outside the experimental error margin. The calculated values that differ from the experimental values by more than twice the error are indicated in red. Experimental data provided by D’Isa et al. [7].**

Flowrate (slm)	SEI (eV molecule <sup>-1</sup> )	Conversion Laminar (%)	Conversion Turbulent (%)	Conversion Experiment (%)
10	0.83	6.9	7.2	6.8 +/- 1.6
10	1.25	8.9	9.1	9.4 +/- 1.6
10	1.66	9.7	9.7	11.5 +/- 1.6
10	2.07	10.6	10.6	13.0 +/- 1.6
20	0.62	4.7	5.4	4.7 +/- 1.6
20	1.03	7.8	9.2	5.3 +/- 1.6
40	0.52	4.6	5.7	3.2 +/- 1.6
40	0.72	6.5	7.6	4.8 +/- 1.6
40	0.83	7.6	8.3	6.3 +/- 1.6

As can be seen from Table 3, turbulence increases the calculated conversion compared to when turbulent heat transfer and turbulent diffusion are ignored (the laminar model). The difference in conversion becomes more pronounced with increasing flow velocity, as is expected from the relative turbulent intensity shown in Figure 11. However, including turbulent diffusion leads to an overestimation of the conversion compared to the experimental values at higher flow rates. This result suggests that our model overestimates turbulent diffusion at higher flow rates. On the other hand, and more importantly, it also suggests that increasing turbulence within the reactor may improve the conversion, opening interesting perspectives for future work.

To assess the influence of turbulent diffusion on the chemistry, turbulent diffusion is ignored for an identical temperature field. Figure 16 illustrates the net reaction rates, the net diffusive transport, and the net convective transport of CO, as a function of radial position, for an axial position of 55 mm, at 40 slm, 1500 W and 1 atm, with (a) and without (b) turbulent diffusion for identical temperature fields. Separating these strongly coupled physics allows us to gain insight into how turbulent diffusion can improve conversion. However, when evaluating whether stronger turbulence may improve conversion in an experimental system, these physics should be coupled, as is presented in Table 3.

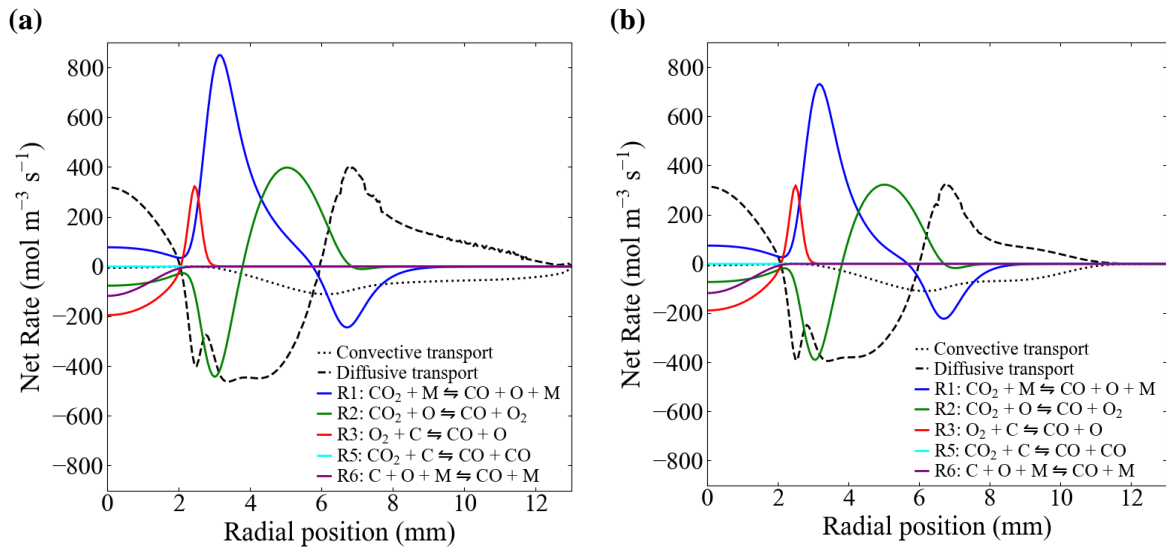


Figure 15 Calculated net reaction rates of reactions involving CO, as well as the net convective and diffusive transport rates, as a function of radial position, at an axial position of 55 mm, for 40 slm, 1500 W and 1 atm. The sign of the reaction rates is chosen so that positive values correspond to net CO production, while a positive sign for net transport corresponds to CO being transported into that region. Turbulent diffusion is considered in (a) and ignored in (b). Both figures are very similar up to  $r = 9$  mm, showing that turbulent diffusion does not affect the plasma chemistry, but above  $r = 9$  mm, net convective transport is higher in (a), demonstrating that CO is transported into the cold outer gas stream by turbulent diffusion, and this is responsible for the difference in calculated CO<sub>2</sub> conversion.

As can be seen from Figure 15, until roughly 2 mm, we observe negligible deviations in the reaction rates and net transport rates between (a) and (b). Indeed, since the temperature field is kept identical in both simulations, only the difference in the concentration of the reactants due to turbulent diffusion can induce differences in the reaction rates. This does not occur, since the kinematic viscosity increases significantly with temperature, reducing the amount of turbulence in the system in the hot regions of the reactor, as observed in the turbulent intensity plot (Figure 11). Hence, the effect of turbulent diffusion on the plasma chemistry is negligible. From 2-9 mm, some deviations in the reaction rates are observed for an identical temperature field, due to a difference in concentration of the species partaking in the reactions. Due to turbulent diffusion, more CO<sub>2</sub> is transported into the plasma edge, whereas more CO and O<sub>2</sub> are transported out of the plasma region. More importantly however, near the reactor edges, i.e., at  $r = 9 - 12$  mm, CO is transported into the cold outer gas stream by turbulent diffusion in (a), whereas this does not occur in (b) where turbulent diffusion is ignored. This small difference in net transport leads to a 75% relative increase in computed conversion when comparing both simulations (i.e., from 3.2%, when not accounting for turbulent diffusion, based on identical temperature fields, to 5.6% when solving fully coupled). These simulation results indicate that turbulent diffusion is important for transporting CO radially into the cold gas stream. This is also illustrated in SI section S.12, where Figure S.18 depicts the difference in mole fraction of CO between the laminar and turbulent solution near the reactor outlet is plotted, showing up to 4% lower mole fraction in the laminar solution, due to the absence of turbulent diffusion. Hence, we postulate that the higher conversion for turbulent flow is attributed to the additional net transport of CO into the cold gas stream by means of turbulent diffusion.

In conclusion, based on our results we hypothesize that increasing the turbulence in a MW CO<sub>2</sub> plasma reactor may improve the conversion by transporting the formed CO to the cold gas stream at the edge of the reactor by means of turbulent diffusion, after which it is convectively transported to the outlet.

## 4. Conclusions

For the first time we developed a 2D axisymmetric thermo-chemical flow model, incorporating turbulent fluid dynamics, heat transfer, transport of species and plasma chemistry, for a MW CO<sub>2</sub> plasma reactor, to gain more insight into the fundamental mechanisms of CO<sub>2</sub> conversion. We specifically investigated the effects of transport of species, as well as turbulence, on various plasma properties, such as the temperature profile, plasma composition, and the CO<sub>2</sub> conversion. We validated our model against experimental values of CO<sub>2</sub> conversion and plasma temperature, illustrating reasonable agreement, certainly keeping in mind that our model does not use any fitting parameters. We demonstrate the need for fully coupling all the physics taken into account in the model and chemistry. Specifically, we stress that deviations in chemical equilibrium make the assumption of LTE in CO<sub>2</sub> MW plasma invalid. Indeed, there are significant deviations in calculated mole fraction spatial profiles with or without accounting for transport of species.

Our model also predicts that the CO<sub>2</sub> conversion happens at the plasma edges. Specifically, net radial diffusion of O atoms towards the plasma edges promotes the CO<sub>2</sub> conversion by the reaction of O + CO<sub>2</sub>. However, some O atoms also diffuse further to the reactor edges and recombine with CO, forming CO<sub>2</sub> again, thereby reducing the net CO<sub>2</sub> conversion.

Finally, we also investigated the effect of turbulence by comparing laminar and turbulent flow solutions. We found that for the current geometry, without nozzle, at 40 slm, the increased heat transfer by turbulence, transports heat to the reactor edges, thereby significantly increasing the cooling in the afterglow. The turbulent thermal conductivity becomes dominant at the reactor edges, allowing for more efficient energy transfer to the quartz tube, which leads to lower temperatures in the afterglow. Last but not least, we show that turbulent diffusion could be an important driver for transporting CO into the cold gas stream at the reactor edges for turbulent flows, after which it is convectively transported to the outlet. However, it must be realized that these are only theoretical model predictions, that have not yet been validated experimentally.

Hence, our model reveals that if turbulent effects can be further enhanced, by changing the reactor design or the gas flow dynamics, the removal of produced CO out of the plasma edges would be further promoted, thus further increasing the overall CO<sub>2</sub> conversion.

## 5. Acknowledgments

This research was supported by the European Research Council (ERC) under the European Union's Horizon 2020 research and innovation programme (grant agreement No 810182 – SCOPE ERC Synergy project). We also thank A. Hecimovic for providing the experimental data about conversion and temperature profiles.

## 6. References

- [1] H. Matthews, S. Wynes, Current global efforts are insufficient to limit warming to 1.5°C, *Science* 376 (2022) 1404-1409. <https://doi.org/10.1126/science.abo3378>.
- [2] B. Szetela, A. Majewska, P. Jamroz, B. Djalilov, R. Salahodjaev, Renewable Energy and CO<sub>2</sub> Emissions in Top Natural Resource Rents Depending Countries: The Role of Governance, *Frontiers in Energy Research* 10 (2022). <https://doi.org/10.3389/fenrg.2022.872941>.
- [3] M. Patel, M. Neelis, D. Gielen, J. Olivier, T. Simmons, J. Theunis, Carbon dioxide emissions from non-energy use of fossil fuels: Summary of key issues and conclusions from the country analyses, *Resources, Conservation and Recycling* 45(3) (2005) 195-209. <https://doi.org/https://doi.org/10.1016/j.resconrec.2005.05.002>.
- [4] S. Valluri, V. Claremboux, S. Kawatra, Opportunities and challenges in CO<sub>2</sub> utilization, *Journal of Environmental Sciences* 113 (2022) 322-344. <https://doi.org/https://doi.org/10.1016/j.jes.2021.05.043>.
- [5] K. Wang, S. Ceulemans, H. Zhang, I. Tsonev, Y. Zhang, Y. Long, M. Fang, X. Li, J. Yan, A. Bogaerts, Inhibiting recombination to improve the performance of plasma-based CO<sub>2</sub> conversion, *Chemical Engineering Journal* 481 (2024) 148684. <https://doi.org/https://doi.org/10.1016/j.cej.2024.148684>.
- [6] C. Du, P. Lu, N. Tsubaki, Efficient and New Production Methods of Chemicals and Liquid Fuels by Carbon Monoxide Hydrogenation, *ACS Omega* 5(1) (2020) 49-56. <https://doi.org/10.1021/acsomega.9b03577>.
- [7] F. D'Isa, E. Carbone, A. Hecimovic, U. Fantz, Performance analysis of a 2.45 GHz microwave plasma torch for CO<sub>2</sub> decomposition in gas swirl configuration, *Plasma Sources Science and Technology* (2020). <https://doi.org/10.1088/1361-6595/abaa84>.
- [8] G. Bonizzoni, E. Vassallo, Plasma physics and technology; industrial applications, *Vacuum* 64(3) (2002) 327-336. [https://doi.org/https://doi.org/10.1016/S0042-207X\(01\)00341-4](https://doi.org/https://doi.org/10.1016/S0042-207X(01)00341-4).
- [9] R.B. Heimann, Plasma spray coating, VCH Verlagsgesellschaft mbH, Weinheim, VCH Publishers, Inc., New York, 1996.
- [10] A. Bogaerts, G. Centi, Plasma Technology for CO<sub>2</sub> Conversion: A Personal Perspective on Prospects and Gaps, *Frontiers in Energy Research* 8 (2020). <https://doi.org/10.3389/fenrg.2020.00111>.
- [11] R. Snoeckx, A. Bogaerts, Plasma technology—a novel solution for CO<sub>2</sub> conversion?, *Chemical Society Reviews* 46(19) (2017) 5805-5863.
- [12] B. Wanten, R. Vertongen, R. De Meyer, A. Bogaerts, Plasma-based CO<sub>2</sub> conversion: How to correctly analyze the performance?, *Journal of Energy Chemistry* 86 (2023) 180-196. <https://doi.org/https://doi.org/10.1016/j.jechem.2023.07.005>.
- [13] R. Vertongen, A. Bogaerts, How important is reactor design for CO<sub>2</sub> conversion in warm plasmas?, *Journal of CO<sub>2</sub> Utilization* 72 (2023) 102510. <https://doi.org/https://doi.org/10.1016/j.jcou.2023.102510>.
- [14] D.C.M. van den Bekerom, J.M.P. Linares, T. Verreycken, E.M. van Veldhuizen, S. Nijdam, G. Berden, W.A. Bongers, M.C.M. van de Sanden, G.J. van Rooij, The importance of thermal dissociation in CO<sub>2</sub> microwave discharges investigated by

power pulsing and rotational Raman scattering, *Plasma Sources Science and Technology* 28(5) (2019) 055015. <https://doi.org/10.1088/1361-6595/aaf519>.

[15] A.J. Wolf, F.J.J. Peeters, P.W.C. Groen, W.A. Bongers, M.C.M. van de Sanden, CO<sub>2</sub> Conversion in Nonuniform Discharges: Disentangling Dissociation and Recombination Mechanisms, *Journal of Physical Chemistry C* 124 (2020) 16806-16819.

[16] A. Bogaerts, A. Berthelot, S. Heijkers, S. Kolev, R. Snoeckx, S. Sun, G. Trenchev, K. Van Laer, W. Wang, CO<sub>2</sub> conversion by plasma technology: insights from modeling the plasma chemistry and plasma reactor design, *Plasma Sources Science and Technology* 26(6) (2017) 063001. <https://doi.org/10.1088/1361-6595/aa6ada>.

[17] N.Y. Babaeva, G.V. Naidis, D.V. Tereshonok, T.V. Chernyshev, L.S. Volkov, M.M. Vasiliev, O.F. Petrov, CO<sub>2</sub> conversion in a microwave plasma torch: 2D vs 1D approaches, *Plasma Sources Science and Technology* 32(5) (2023) 054001. <https://doi.org/10.1088/1361-6595/acce66>.

[18] N. den Harder, D.C.M. van den Bekerom, R.S. Al, M.F. Graswinckel, J.M. Palomares, F.J.J. Peeters, S. Ponduri, T. Minea, W.A. Bongers, M.C.M. van de Sanden, G.J. van Rooij, Homogeneous CO<sub>2</sub> conversion by microwave plasma: Wave propagation and diagnostics, *Plasma Processes and Polymers* 14(6) (2017) 1600120. <https://doi.org/https://doi.org/10.1002/ppap.201600120>.

[19] E. Carbone, F. D'Isa, A. Hecimovic, U. Fantz, Analysis of the C<sub>2</sub> Swan bands as a thermometric probe in CO<sub>2</sub> microwave plasmas, *Plasma Sources Science and Technology* 29(5) (2020) 055003. <https://doi.org/10.1088/1361-6595/ab74b4>.

[20] A. van de Steeg, P. Viegas, A. Silva, T. Butterworth, A. van Bavel, J. Smits, P. Diomede, M. van de Sanden, G. van Rooij, Redefining the Microwave Plasma-Mediated CO<sub>2</sub> Reduction Efficiency Limit: The Role of O–CO<sub>2</sub> Association, *ACS Energy Letters* 6(8) (2021) 2876-2881. <https://doi.org/10.1021/acsenergylett.1c01206>.

[21] P. Viegas, L. Vialetto, A.J. Wolf, F.J.J. Peeters, P.W.C. Groen, T.W.H. Righart, W.A. Bongers, M.C.M. van de Sanden, P. Diomede, Insight into contraction dynamics of microwave plasmas for CO<sub>2</sub> conversion from plasma chemistry modelling, *Plasma Sources Science and Technology* 29(10) (2020) 105014. <https://doi.org/10.1088/1361-6595/abb41c>.

[22] S. Van Alphen, A. Hecimovic, C.K. Kiefer, U. Fantz, R. Snyders, A. Bogaerts, Modelling post-plasma quenching nozzles for improving the performance of CO<sub>2</sub> microwave plasmas, *Chemical Engineering Journal* 462 (2023) 142217. <https://doi.org/https://doi.org/10.1016/j.cej.2023.142217>.

[23] E.R. Mercer, S. Van Alphen, C.F.A.M. van Deursen, T.W.H. Righart, W.A. Bongers, R. Snyders, A. Bogaerts, M.C.M. van de Sanden, F.J.J. Peeters, Post-plasma quenching to improve conversion and energy efficiency in a CO<sub>2</sub> microwave plasma, *Fuel* 334 (2023) 126734. <https://doi.org/https://doi.org/10.1016/j.fuel.2022.126734>.

[24] G. Trenchev, S. Kolev, W. Wang, M. Ramakers, A. Bogaerts, CO<sub>2</sub> Conversion in a Gliding Arc Plasmatron: Multidimensional Modeling for Improved Efficiency, *The Journal of Physical Chemistry C* 121(44) (2017) 24470-24479. <https://doi.org/10.1021/acs.jpcc.7b08511>.

- [25] M.I. Boulos, P.L. Fauchais, E. Pfender, Fundamental Concepts in Gaseous Electronics, in: M.I. Boulos, P.L. Fauchais, E. Pfender (Eds.), Handbook of Thermal Plasmas, Springer International Publishing, Cham, 2023, pp. 139-180.  
[https://doi.org/10.1007/978-3-030-84936-8\\_4](https://doi.org/10.1007/978-3-030-84936-8_4).
- [26] V. Kotov, P.M.J. Koelman, Plug flow reactor model of the plasma chemical conversion of CO<sub>2</sub>, Plasma Sources Science and Technology 28(9) (2019) 095002.  
<https://doi.org/10.1088/1361-6595/ab3774>.
- [27] R. Elahi, E.M. Simasiku, J.P. Trelles, Computational modeling of CO<sub>2</sub> conversion by a solar-enhanced microwave plasma reactor, Plasma Sources Science and Technology 32(6) (2023) 065018. <https://doi.org/10.1088/1361-6595/acde08>.
- [28] T. Kozák, A. Bogaerts, Splitting of CO<sub>2</sub> by vibrational excitation in non-equilibrium plasmas: a reaction kinetics model, Plasma Sources Science and Technology 23(4) (2014) 045004. <https://doi.org/10.1088/0963-0252/23/4/045004>.
- [29] T. Kozák, A. Bogaerts, Evaluation of the energy efficiency of CO<sub>2</sub> conversion in microwave discharges using a reaction kinetics model, Plasma Sources Science and Technology 24 (2014). <https://doi.org/10.1088/0963-0252/24/1/015024>.
- [30] O. Biondo, C. Fromentin, T. Silva, V. Guerra, G. van Rooij, A. Bogaerts, Insights into the limitations to vibrational excitation of CO<sub>2</sub>: validation of a kinetic model with pulsed glow discharge experiments, Plasma Sources Science and Technology 31(7) (2022) 074003. <https://doi.org/10.1088/1361-6595/ac8019>.
- [31] L.D. Pietanza, O. Guaitella, V. Aquilanti, I. Armenise, A. Bogaerts, M. Capitelli, G. Colonna, V. Guerra, R. Engeln, E. Kustova, Advances in non-equilibrium CO<sub>2</sub> plasma kinetics: A theoretical and experimental review, The European Physical Journal D 75(9) (2021) 237.
- [32] V. Vermeiren, A. Bogaerts, Plasma-Based CO<sub>2</sub> Conversion: To Quench or Not to Quench?, The Journal of Physical Chemistry C 124(34) (2020) 18401-18415.  
<https://doi.org/10.1021/acs.jpcc.0c04257>.
- [33] V. Kotov, C.K. Kiefer, A. Hecimovic, Validation of the thermo-chemical approach to modelling of the CO<sub>2</sub> conversion in sub-atmospheric pressure microwave gas discharges, Plasma Sources Science and Technology (2024).
- [34] F. Seibold, P. Ligrani, B. Weigand, Flow and heat transfer in swirl tubes — A review, International Journal of Heat and Mass Transfer 187 (2022) 122455.  
<https://doi.org/https://doi.org/10.1016/j.ijheatmasstransfer.2021.122455>.
- [35] R. Resiga, S. Muntean, C. Tanasa, A. Bosioc, Three-Dimensional versus Two-Dimensional Axisymmetric Analysis for Decelerated Swirling Flows, 2006.
- [36] M. Tatar, V. Vashisth, M. Iqbal, T. Butterworth, G. van Rooij, R. Andersson, Analysis of a plasma reactor performance for direct nitrogen fixation by use of three-dimensional simulations and experiments, Chemical Engineering Journal 497 (2024) 154756. <https://doi.org/https://doi.org/10.1016/j.cej.2024.154756>.
- [37] A. Hecimovic, F.A. D'Isa, E. Carbone, U. Fantz, Enhancement of CO<sub>2</sub> conversion in microwave plasmas using a nozzle in the effluent, Journal of CO<sub>2</sub> Utilization 57 (2022) 101870. <https://doi.org/https://doi.org/10.1016/j.jcou.2021.101870>.
- [38] A. Roberts, Calculus Volume 2, 2022.

- [39] S. Maerivoet, I. Tsonev, J. Slaets, F. Reniers, A. Bogaerts, Coupled Multi-Dimensional Modelling of Warm Plasmas: Application and Validation for an Atmospheric Pressure Glow Discharge in Co<sub>2</sub>/Ch<sub>4</sub>/O<sub>2</sub>, 2024. <https://doi.org/10.2139/ssrn.4705553>.
- [40] W.P. Reed, Standard Reference Material 739 - Fused Silica Thermal Expansion, National Institute of Standards & Technology, Gaithersburg, 1991, p. 2.
- [41] C.B. Batchelor, G., An introduction to fluid dynamics, Cambridge University Press, Cambridge, 2000.
- [42] COMSOL, Comsol Multiphysics 6.0 CFD Module User's Guide.
- [43] F. Menter, M. Kuntz, R.B. Langtry, Ten years of industrial experience with the SST turbulence model, Heat and Mass Transfer 4 (2003).
- [44] W. Li, Y. Li, C. Li, L. Zhu, X. Chen, A numerical Investigation on Schardin's Problem Using a Quasi-DNS Solver, Journal of Physics: Conference Series 2235(1) (2022) 012025. <https://doi.org/10.1088/1742-6596/2235/1/012025>.
- [45] COMSOL, Comsol Multiphysics 6.0 Chemical Reaction Engineering Module User's Guide.
- [46] Molecular Transport, Chemically Reacting Flow 2003, pp. 487-539. <https://doi.org/https://doi.org/10.1002/0471461296.ch12>.
- [47] P.D. Neufeld, A.R. Janzen, R.A. Aziz, Empirical Equations to Calculate 16 of the Transport Collision Integrals  $\Omega(l, s)^*$  for the Lennard-Jones (12-6) Potential, The Journal of Chemical Physics 57(3) (1972) 1100-1102. <https://doi.org/10.1063/1.1678363>.
- [48] W.M. Kays, Turbulent Prandtl Number—Where Are We?, Journal of Heat Transfer 116(2) (1994) 284-295. <https://doi.org/10.1115/1.2911398>.
- [49] D.M.G. Gregory P. Smith, Michael Frenklach, Nigel W. Moriarty, Boris Eiteneer, Mikhail Goldenberg, C. Thomas Bowman, Ronald K. Hanson, Soonho Song, William C. Gardiner, Jr., Vitali V. Lissianski, and Zhiwei Qin, GRI-Mech 3.0, 2024. [http://www.me.berkeley.edu/gri\\_mech/](http://www.me.berkeley.edu/gri_mech/).
- [50] A. Berthelot, A. Bogaerts, Modeling of plasma-based CO<sub>2</sub> conversion: lumping of the vibrational levels, Plasma Sources Science and Technology 25(4) (2016) 045022. <https://doi.org/10.1088/0963-0252/25/4/045022>.
- [51] M.S. Silberberg, P. Amateis, R. Venkateswaran, L. Chen, Chemistry: The molecular nature of matter and change, McGraw-Hill New York 2006.
- [52] A.W. Cook, Enthalpy diffusion in multicomponent flows, Physics of Fluids 21(5) (2009). <https://doi.org/10.1063/1.3139305>.
- [53] B.J. McBride, M.J. Zehe, S.D. Gordon, NASA Glenn Coefficients for Calculating Thermodynamic Properties of Individual Species, 2002.
- [54] P. Viegas, L. Vialetto, A.W. van de Steeg, A.J. Wolf, W.A. Bongers, G.J. van Rooij, M.C.M. van de Sanden, P. Diomedè, F.J.J. Peeters, Resolving discharge parameters from atomic oxygen emission, Plasma Sources Science and Technology 30(6) (2021) 065022. <https://doi.org/10.1088/1361-6595/ac04bd>.

- [55] F. Menter, Zonal Two Equation k- $\omega$  Turbulence Models For Aerodynamic Flows, 23rd Fluid Dynamics, Plasmadynamics, and Lasers Conference. <https://doi.org/10.2514/6.1993-2906>.
- [56] A.B. Murphy, Thermal plasmas in gas mixtures, Journal of Physics D: Applied Physics 34(20) (2001) R151. <https://doi.org/10.1088/0022-3727/34/20/201>.
- [57] W. Bongers, H. Bouwmeester, B. Wolf, F. Peeters, S. Welzel, D. van den Bekerom, N. den Harder, A. Goede, M. Graswinckel, P.W. Groen, J. Kopecki, M. Leins, G. van Rooij, A. Schulz, M. Walker, R. van de Sanden, Plasma-driven dissociation of CO<sub>2</sub> for fuel synthesis, Plasma Processes and Polymers 14(6) (2017) 1600126. <https://doi.org/https://doi.org/10.1002/ppap.201600126>.
- [58] S. Maerivoet, I. Tsonev, J. Slaets, F. Reniers, A. Bogaerts, Coupled multi-dimensional modelling of warm plasmas: Application and validation for an atmospheric pressure glow discharge in CO<sub>2</sub>/CH<sub>4</sub>/O<sub>2</sub>, Chemical Engineering Journal 492 (2024) 152006. <https://doi.org/https://doi.org/10.1016/j.cej.2024.152006>.
- [59] M.S. Siddiqui, A. Rasheed, T. Kvamsdal, M. Tabib, Effect of Turbulence Intensity on the Performance of an Offshore Vertical Axis Wind Turbine, Energy Procedia 80 (2015) 312-320. <https://doi.org/https://doi.org/10.1016/j.egypro.2015.11.435>.

# Supplementary information: Influence of radial transport and turbulent effects on CO<sub>2</sub> conversion in a microwave plasma reactor: Insights from a thermo-chemical flow model.

Helder M.S. Van Poyer, Ivan Tsonev, Stein J.R. Maerivoet, Matthias Albrechts, Annemie Bogaerts

Research Group PLASMANT, Department of Chemistry, University of Antwerp, Universiteitsplein 1, BE-2610 Wilrijk-Antwerp, Belgium

## S.1. Plasma size measurements as a function of input power

The plasma size is adopted from the experiments at 1 bar and 20 slm and applied in the model for all different flow rates. Both the length and width of the plasma are almost independent of flow rate.

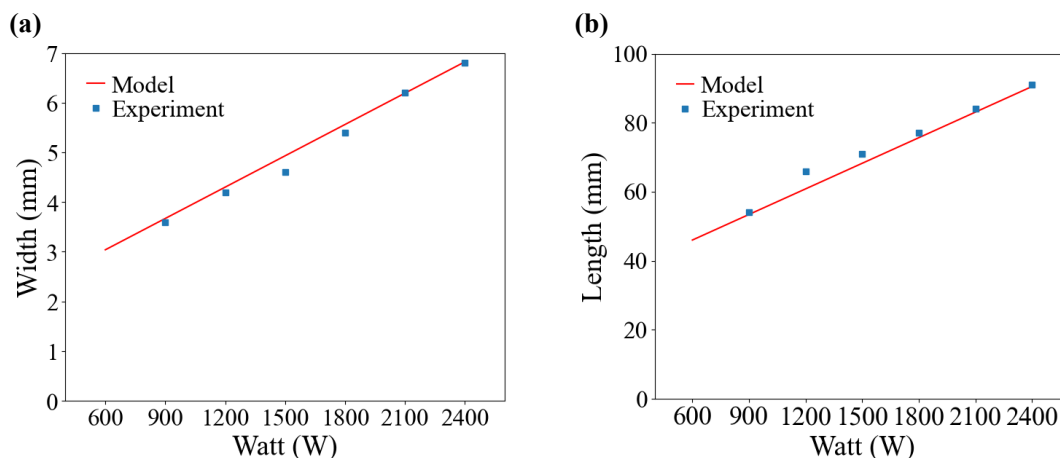


Figure S.1. Plasma width (a) and length (b) as digitized from measured data by D'Isa for 1 bar and 20 slm (blue squares) [1] compared to interpolation used in the model to describe the heat source based on the input power (red).

The values of X and Y of figure 2 in the main paper correspond with the plasma width and length for a given input power presented in Figure S.1. We applied an interpolation function to present the plasma size in each dimension for the given input powers, since the dependence on flow rate is negligible. For the full experimental work, we refer to [1]. Note that an increase in plasma power leads to an increase in the volume of the heat source, and consequently, deposited power and power density are not directly proportional.

## S.2. Meshing of the simulation domain

### S.2.1. 3D Mesh

The 3D mesh consists of 17,792,576 mesh elements, of which 15,910,456 are tetrahedral elements, 1,882,120 are prisms, 198,312 are triangles 3400 are quads, 340 are edge elements and 10 are vertex elements. The mesh size is illustrated in Figure S.2.

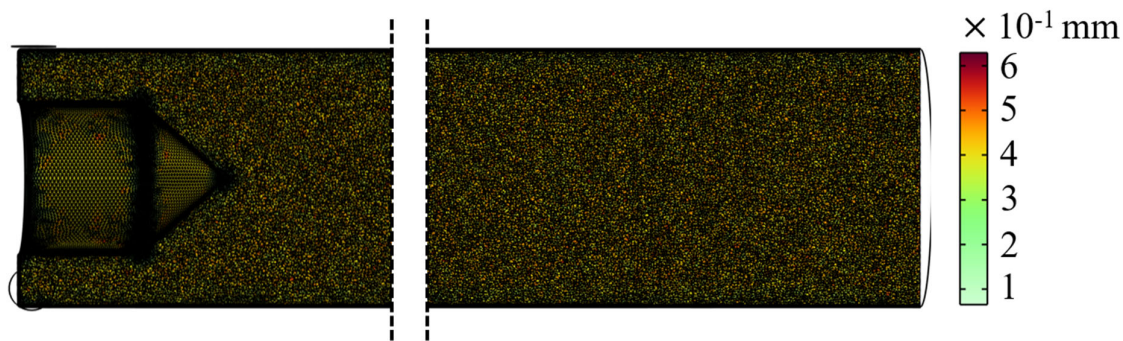


Figure S.2. Mesh plot of the 3D fluid domain, representing the mesh size.

The mesh was refined by reducing the maximum and minimum element size by 50% until negligible (<1%) changes in maximum velocity in the reactor were obtained, and the maximum element size was set to be 0.4 mm and the minimum element size to 0.1 mm.

### S.2.2. 2D axi-symmetric mesh

The 2D axisymmetric mesh consists of 1,034,434 mesh elements, of which 983,714 are triangles, 50,720 are quads, 8523 are edge elements and 9 are vertex elements. The mesh size is illustrated in Figure S.3.

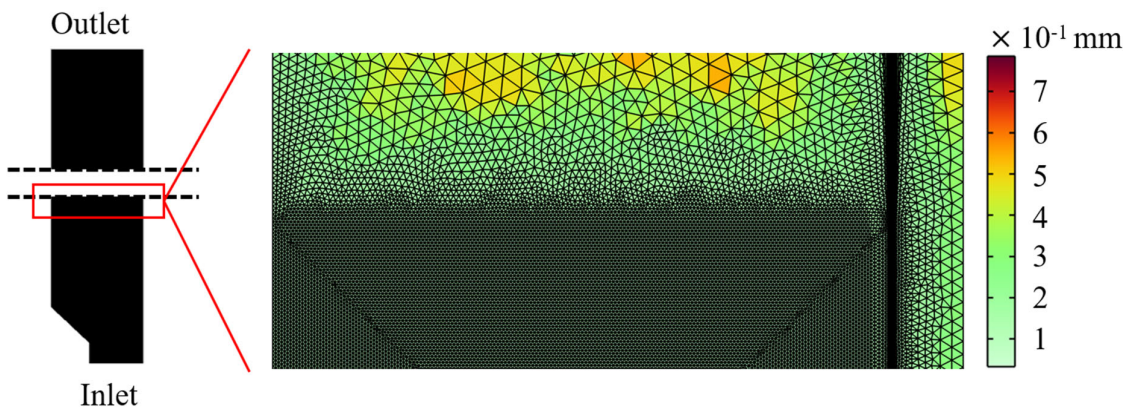


Figure S.3. Mesh plot of the 3D fluid domain, representing the mesh size of the region where the mesh size transitions.

From Figure S.3 it is apparent that the mesh is too dense to plot at once, the inlet region of the mesh was plotted, to show the mesh density. The mesh was first refined by reducing the maximum and minimum element size by 50% until negligible changes (<1%) in global variables (e.g., maximum temperature, maximum velocity magnitude and conversion) were observed. The mesh was further refined until negligible changes in local values (local reaction and transport rates) were observed.

The region from the inlet to an axial position of 16 cm has a finer mesh, with the maximum mesh element size set to 0.0772 mm and the minimum mesh element size set to  $2.9 \times 10^{-4}$  mm. The longest heat source at 2400 W is well below 10 cm as can be seen from Figure S.1 (b). The afterglow region to the outlet is meshed with the maximum element size set to 0.189 mm and the minimum element size

set to  $2.18 \times 10^{-3}$  mm. In the afterglow the temperature gradients are significantly less steep, requiring a less dense mesh.

Finally, in order to validate whether our mesh is fine enough to resolve the boundary layer near the wall, we used the distance to the cell center in viscous units, which is less than 0.5 for all of our simulation results, as suggested for modelling the low-Reynolds formulation of the boundary layers in [2].

### S.3. Thermophysical properties of the quartz tube

Figure S.4 presents the thermal conductivity (left) and the heat capacity (right) of the quartz tube, as a function of temperature.

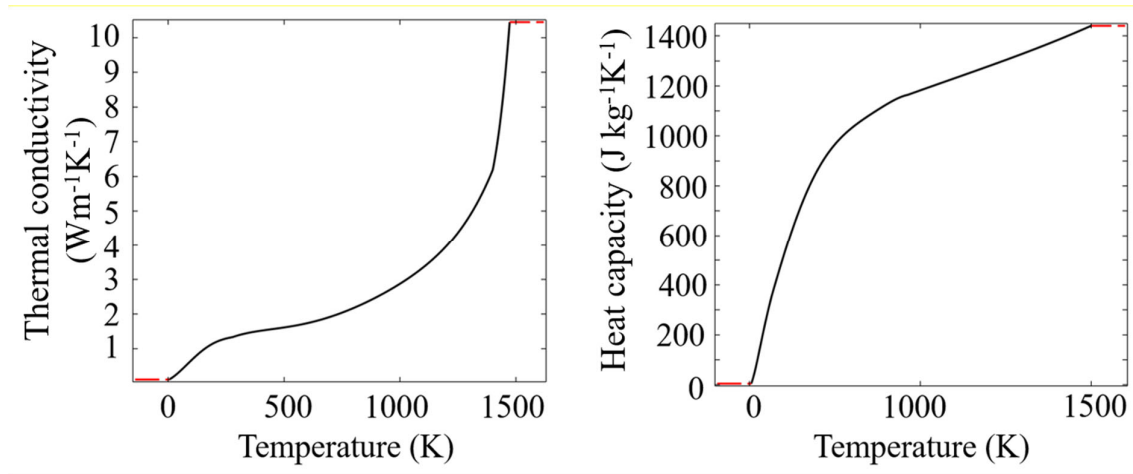


Figure S.4. Thermophysical properties of the quartz tube as a function of temperature: thermal conductivity (left) and heat capacity (right).

Nearly all multi-dimensional CO<sub>2</sub> models from literature do not solve for surface-to-ambient radiation (e.g., [3-6]). In contrast to these models, we considered surface-to-ambient radiation in our model, by employing the Stefan-Boltzmann law at the HA-boundary (see Table 2 of the main paper) in the 2D axisymmetric model. We found that applying the surface-to-ambient radiation at the AH boundary significantly reduces the gas temperature at the edges of the fluid domain (BG). This is due to more efficient heat dissipation through the quartz wall out of the simulation domain compared to only convective heat loss at this boundary, as can be seen in Figure S.5

Temperature of the outside of the quartz tube as a function of length for different emission coefficients.

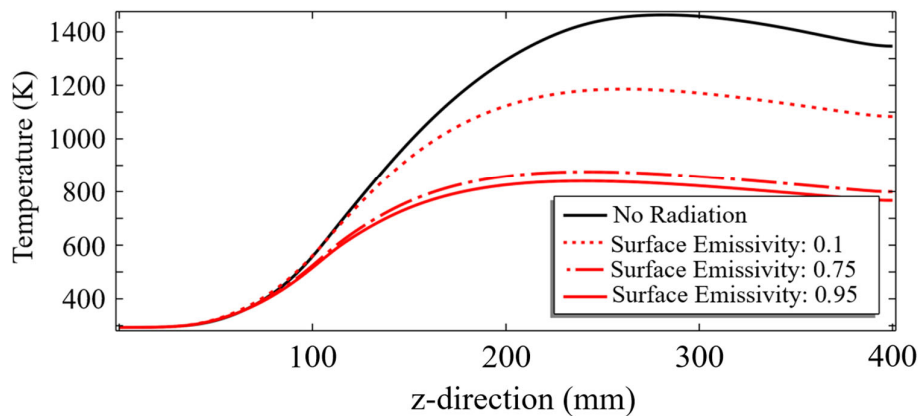


Figure S.5. Axial temperature profile at the HA boundary for different emission coefficients, for 10 slm, 1500 W and 1 atm.

The reported surface emissivity for quartz tubes varies in literature from 0.67-0.95 [7-9]. We applied a surface emissivity of 0.75 in our model. As can be seen from Figure S.5, higher values of this coefficient have a negligible effect on the gas temperature near the quartz wall. The temperature variation between the inner and outer boundary of the quartz tube is never more than 25 K for the conditions under study. Generally, one could take the temperature at the edge of the fluid domain as a proxy for the temperature at the edge of the simulation domain and avoid modelling the quartz tube.

## S.4. Turbulent viscosity and SST variables

The turbulent viscosity,  $\mu_T$  used in Eq.5 in section 2.2 of the main paper is defined as [10]:

$$\mu_T = \frac{a_1 k}{\max(a_1 \omega, S f_{v2})} \quad (1)$$

With  $f_{v2}$ , a blending function, defined as:

$$f_{v2} = \tanh(\theta_2^2) \quad (2)$$

$$\theta_2 = \max\left(\frac{2\sqrt{k}}{\beta_0^* \omega l_w}, \frac{500 \mu}{\rho \omega l_w^2}\right) \quad (3)$$

With  $S$  the measure of the strain rate and  $l_w$  the distance closest to the wall.  $\beta_0^*$  is a model constant. The model constants are defined through an interpolation function:

$$\Phi = f_{v1} \Phi_1 + (1 - f_{v1}) \Phi_2 \quad \text{for} \quad \Phi = \beta, \gamma, \sigma_k, \sigma_\omega \quad (4)$$

Furthermore, the blending function  $f_{v1}$  is defined as:

$$f_{v1} = \tanh(\theta_1^4) \quad (5)$$

$$\theta_1 = \min\left[\max\left(\frac{\sqrt{k}}{\beta_0^* \omega l_w}, \frac{500 \mu}{\rho \omega l_w^2}\right), \frac{4\rho\sigma_{\omega 2} k}{CD_{k\omega} l_w^2}\right] \quad (6)$$

$$CD_{k\omega} = \max\left(\frac{2\rho\sigma_{\omega 2}}{\omega} \nabla\omega \cdot \nabla k, 10^{-10}\right) \quad (7)$$

The constants for the model used in equation 1-7 are  $\beta^* = 0.09$ ,  $a_1 = 5/9$ ,  $\beta_1 = 3/40$ ,  $\sigma_{\omega 1} = 0.85$ ,  $\sigma_{\omega 2} = 0.5$ ,  $a_2 = 0.44$ ,  $\beta_2 = 0.0828$ ,  $\sigma_{k2} = 1$  and  $\sigma_{\omega 2} = 0.856$ , taken from Menter et al. [11]. For further information on the SST model, we refer to [2, 10].

## S.5 NASA polynomials for the different species

The thermophysical properties for each species are determined using the nine-term NASA Glenn polynomials which are valid up to 20 000 K [12]. The equations for the polynomials are as follows:

$$C_p^\circ(T) = R \left( a_1 T^{-2} + \frac{a_2}{T} + a_3 + a_4 T + a_5 T^2 + a_6 T^3 + a_7 T^4 \right) \quad (8)$$

$$H^\circ(T) = RT \left( -a_1 T^{-2} + a_2 \frac{\ln T}{T} + a_3 + a_4 \frac{T}{2} + a_5 \frac{T^2}{3} + a_6 \frac{T^3}{4} + a_7 \frac{T^4}{5} + \frac{b_1}{T} \right) \quad (9)$$

$$S^\circ(T) = R \left( -a_1 \frac{T^{-2}}{2} - \frac{a_2}{T} + a_3 \ln T + a_4 T + a_5 \frac{T^2}{2} + a_6 \frac{T^3}{3} + a_7 \frac{T^4}{4} + b_2 \right) \quad (10)$$

With  $C_p^\circ(T)$  the molar heat capacity at constant pressure, at temperature  $T$ ,  $H^\circ(T)$  the molar enthalpy at temperature  $T$  relative to the molar enthalpy at 0 K, and  $S^\circ(T)$  the entropy at temperature  $T$ , all for standard state. The standard state, denoted with  $^\circ$ , refers to the standard state of the ideal gas at 1 atm.

## S.6. Calculation of the thermal conductivity and dynamic viscosity of species i:

Equation 11 represents the calculation of the thermal conductivity of species i [13]:

$$k_{m,i} = 2.669 \times 10^{-6} \frac{\sqrt{TM_i \times 10^3}}{\sigma_i^2 \Omega_k} \times \frac{1.15C_{p,i} + 0.88R_g}{M_i} \quad (11)$$

$$\Omega_k = \frac{b_1}{(T^*)^{b_2}} + \frac{b_3}{\exp(b_4 T^*)} + \frac{b_5}{\exp(b_6 T^*)} + \frac{4.998 \cdot 10^{-40} \mu_{D,i}^4}{k_b^2 T^* \sigma_i^6}, \quad T^* = T \frac{\varepsilon_i}{k_b} \quad (12)$$

With the characteristic length of the Lennard-Jones potential represented by  $\sigma_i$  and the dimensionless collision integral indicated by  $\Omega_k$ .  $C_{p,i}$  the heat capacity at constant pressure of the individual species,  $M_i$  the molar mass of the individual species and  $R_g$  is the ideal gas constant. In equation 12,  $b_x$  are empirical constants,  $\mu_{D,i}$  is the dipole constant of species  $i$  (D),  $\varepsilon_i$  is the potential energy minimum value (J) and  $k_b$  is Boltzmann's constant (J K<sup>-1</sup>). Finally,  $\mu$  and  $\rho$  also depend on the chemical composition. The former is calculated using:

$$\mu = \sum_{i=1}^n \frac{\mu_i}{1 + \frac{1}{x_i} \sum_{j=1, j \neq i}^n x_j \phi_{ij}}, \quad \phi_{ij} = \frac{(1 + (\mu_i/\mu_j)^{0.5} (M_j/M_i)^{0.25})^2}{(4/\sqrt{2})(1 + M_i/M_j)^{0.5}} \quad (13)$$

$$\mu_i = 2.669 \times 10^{-6} \frac{\sqrt{TM_i \times 10^3}}{\sigma_i^2 \Omega_D} \quad (14)$$

$$\Omega_D = \frac{b_1}{(T^*)^{b_2}} + \frac{b_3}{\exp(b_4 T^*)} + \frac{b_5}{\exp(b_6 T^*)} + \frac{4.998 \times 10^{-40} \mu_{D,i}^4}{k_b^2 T^* \sigma_i^6}, \quad T^* = T \frac{k_b}{\varepsilon_i} \quad (15)$$

With  $x_i$  is the molar fraction,  $\mu_i$  the dynamic viscosity of species  $i$ ,  $\Omega_D$  the dimensionless collision integral and  $\rho$  the density [13].

### S.7. Full experimental dataset compared to the modelled range.

As discussed in section 3.1 of the main paper, our model is not yet able to reproduce the CO<sub>2</sub> conversion in the full experimental range of SEI values. Figure S.6 presents the full SEI range, as provided by D'Isa et al. [1].

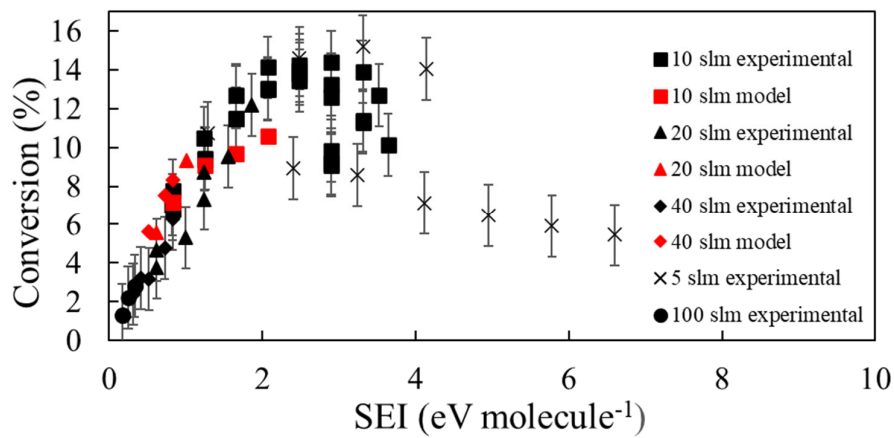


Figure S.6 Full experimental dataset as presented by D'Isa et al. [10], compared with the conditions modelled in the main paper.

Our model was not validated for 100 slm flow rate, since the observed conversion is in the order of magnitude of the error bars, and furthermore, no temperature measurements were provided for this flow rate. As discussed in section 3.1 of the main paper, higher SEI measurements could not yet be reproduced by our model, due to reactions persisting until the end of the simulation domain.

### S.8. Sensitivity analysis heat source expanded

It was reported by Viegas et al. that optical contraction can happen in CO<sub>2</sub> plasmas below 150 mbar. The effect is not reported at higher pressures, and Vialetto et al. showed that at 250 mbar, the normalized electron number density and emission intensity profile overlap; nevertheless possible optical contraction is considered here [14]. Viegas et al. suggested a scaling factor of 1.6 when assessing the size of the plasma, that is, the measured width should be multiplied by 1.6 to get the actual plasma width. In our model, the plasma is approximated as a heat source, and therefore, the heat source width is multiplied by 1.5 for identical input power of 1500W at 10 slm and 40 slm. The corresponding power deposition profiles are plotted in Figure S.7.

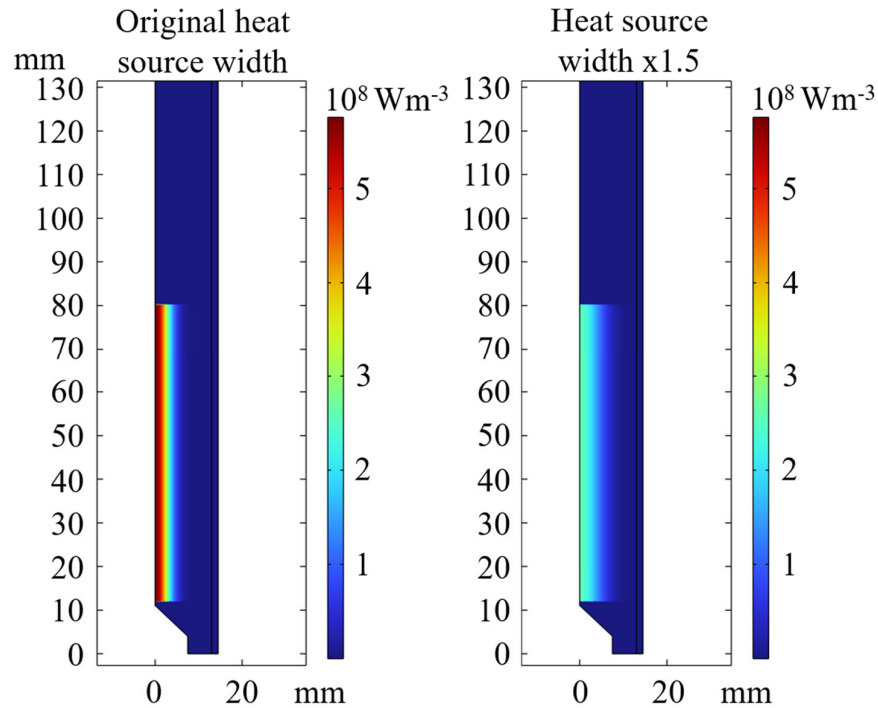


Figure S.7. Heat source profile according to measured data (left) and radially expanded by a factor 1.5 (right)

As can be seen from figure S.8 expanding the power deposition profile by a factor 1.5 actually increases correspondence with the experiment, as the core temperature drops, which reduces our overestimation of the temperature. The conversion decreases from 10.6% to 10.4% and is thus clearly less sensitive to this change.

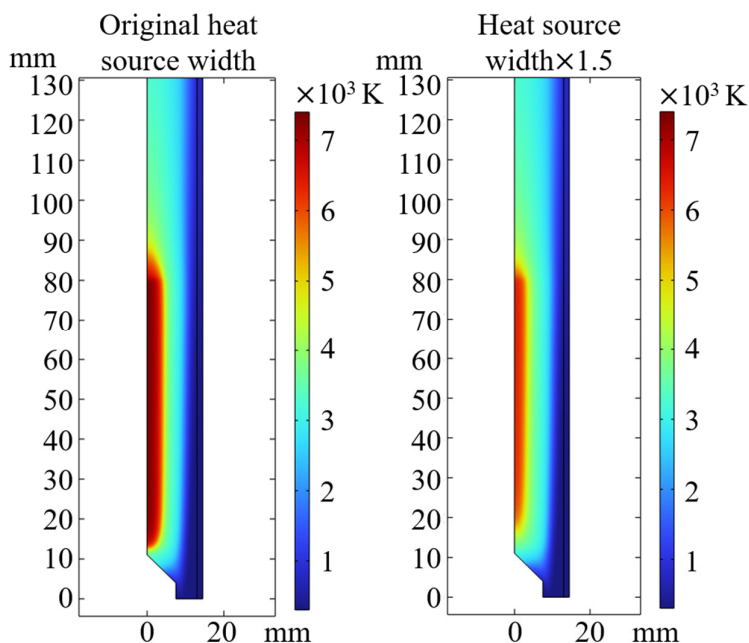


Figure S.8. Temperature profile for original heat source (left) and radially expanded heat source (right) for 10 slm and 1500 W.

However, expanding the heat source at higher flow rates actually results in the gas not being heated efficiently. It should be noted that the temperature scale in Figure S.9 (right) was adapted for clarity.

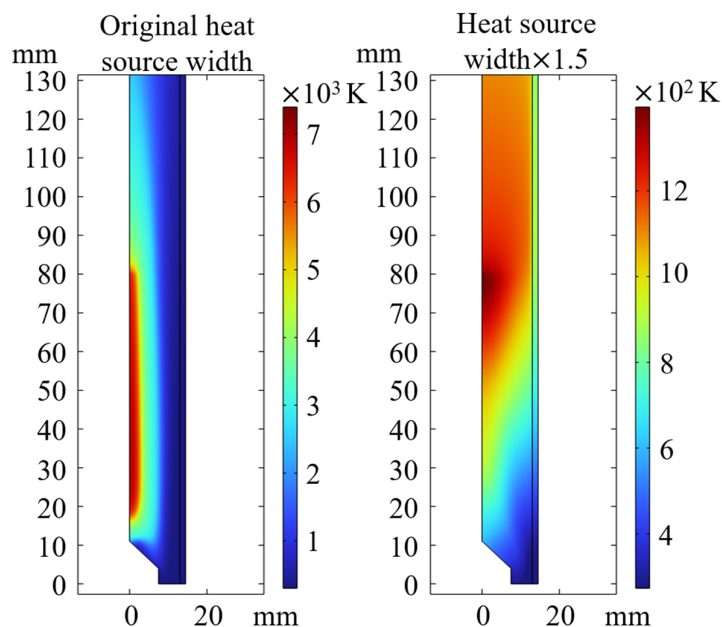


Figure S.9. Temperature profile for original heat source (left) and radially expanded heat source (right) for 40 slm and 1500 W.

Clearly, at 40 slm, drastic changes in the heat source have a significant effect on both temperature profile and conversion, since the temperature does not increase sufficiently enough to dissociate  $\text{CO}_2$  at 40 slm, 1500 W for the broader heat source. Therefore, we can conclude that even though fitting the heat source might lead to better agreement with experiment in some conditions, we adhere to the measured plasma dimensions, assuming optical contraction is irrelevant at higher pressure.

### S.9 Sensitivity analysis for the initial turbulent intensity

It is known from literature that Menter's SST models are sensitive to the boundary conditions for the specific dissipation rate ( $\omega$ ) [11]. Our models fully resolve the boundary layer using a low-Reynolds formulation at the wall, which is consistent with the no-slip condition. This is checked based on the distance to the cell center in viscous units, as suggested in [2]. The outlet boundary condition is sufficiently far away from the heat source in the model and is therefore assumed to have limited effect.

Lastly, at the inlet both  $k$  and  $\omega$  need to be specified. These results might affect the results further in the domain. Both  $k$  and  $\omega$  can be averaged over the  $\phi$ -direction analogous to the velocity (see section 2.1 of the main paper), and the results over the inlet for 40 slm are plotted in figure S.10.

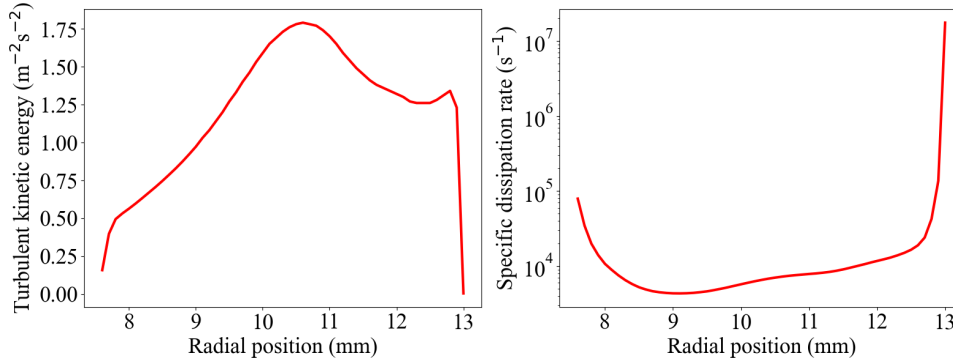


Figure S.10. Turbulent kinetic energy (left) and specific dissipation rate (right) for 40 slm at the inlet of the 2D domain, derived by averaging over the  $\phi$ -direction in the 3D model.

Alternatively, a value for  $k$  ( $0.005 \text{ m}^2 \text{ s}^{-2}$ ) and  $\omega$  ( $20 \text{ s}^{-1}$ ) can be chosen at the inlet, as is done in the main paper. This means that both the turbulent kinetic energy and the turbulent dissipation rate vary over two orders of magnitude at the inlet. We compare both methods at the highest flow rate, which corresponds to the strongest turbulence. Figure S.11 shows the relative turbulent intensity for the chosen values (left) and the interpolated values from the 3D model (right).

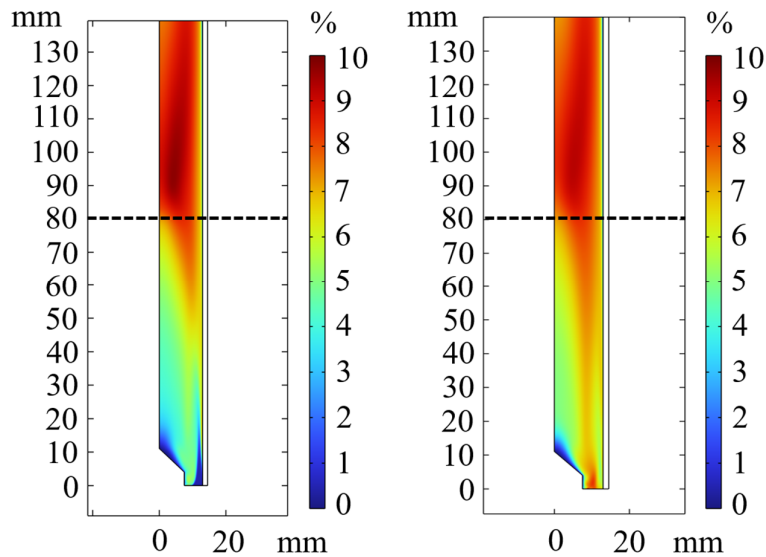


Figure S.11 Comparison of relative turbulent intensity for fixed values of  $k$  and  $\omega$  (left) and for the interpolated values (right) for 40 slm and 1500 W.

As can be seen in Figure S.11, the turbulent intensity profiles are somewhat different for both cases. This results in variations in the core plasma temperature, however, as discussed in the main paper (section 3.2) and in the SI section S.8, significant deviations in the temperature profile are required to really affect the conversion. Moreover, as discussed in section 3.7.3 of the main paper, turbulence needs to be significantly enhanced to promote conversion, as indicated by Table 3 of the main paper. The temperature profile is plotted for 40 slm and 1500 W in Figure S.12.

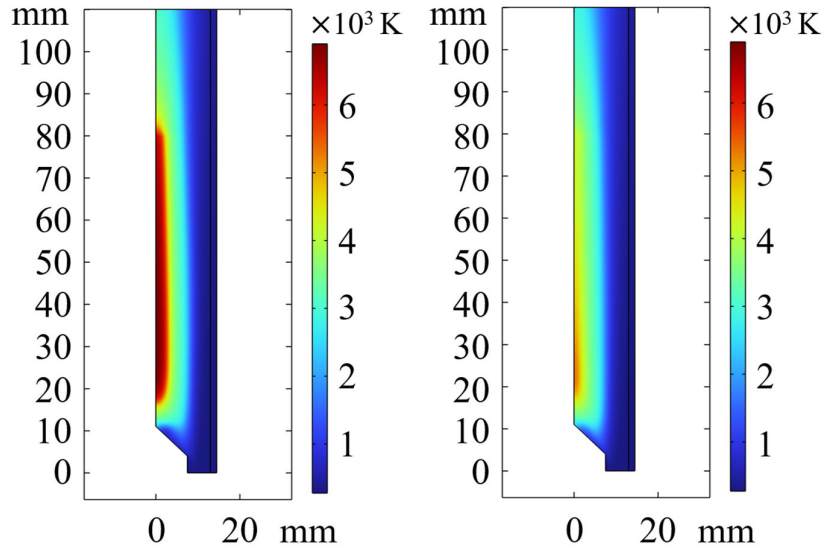


Figure S.12 Comparison of temperature profile for fixed values of  $k$  and  $\omega$  (left) and for the interpolated values (right) for 40 slm and 1500 W.

As can be seen in the figure, there is a strong drop in core plasma temperature when the interpolated values for  $k$  and  $\omega$  are employed (right). Nevertheless, as discussed in section 3.2 of the main paper, the conversion shows only limited sensitivity with respect to the temperature profile. Moreover, as discussed in section 3.5 of the main paper, all C atoms are created by dissociation of CO, and diffusion of C atoms can only cause additional conversion upon reacting with CO<sub>2</sub> according to R5, which does not occur. The core plasma temperature, which determines the dissociation rate of CO, is thus of lesser importance, as shown in section 3.2 of the main paper. Moreover, at lower flow rates, as well as at higher SEI, the effects become significantly less pronounced, as plotted in Figure S.13.

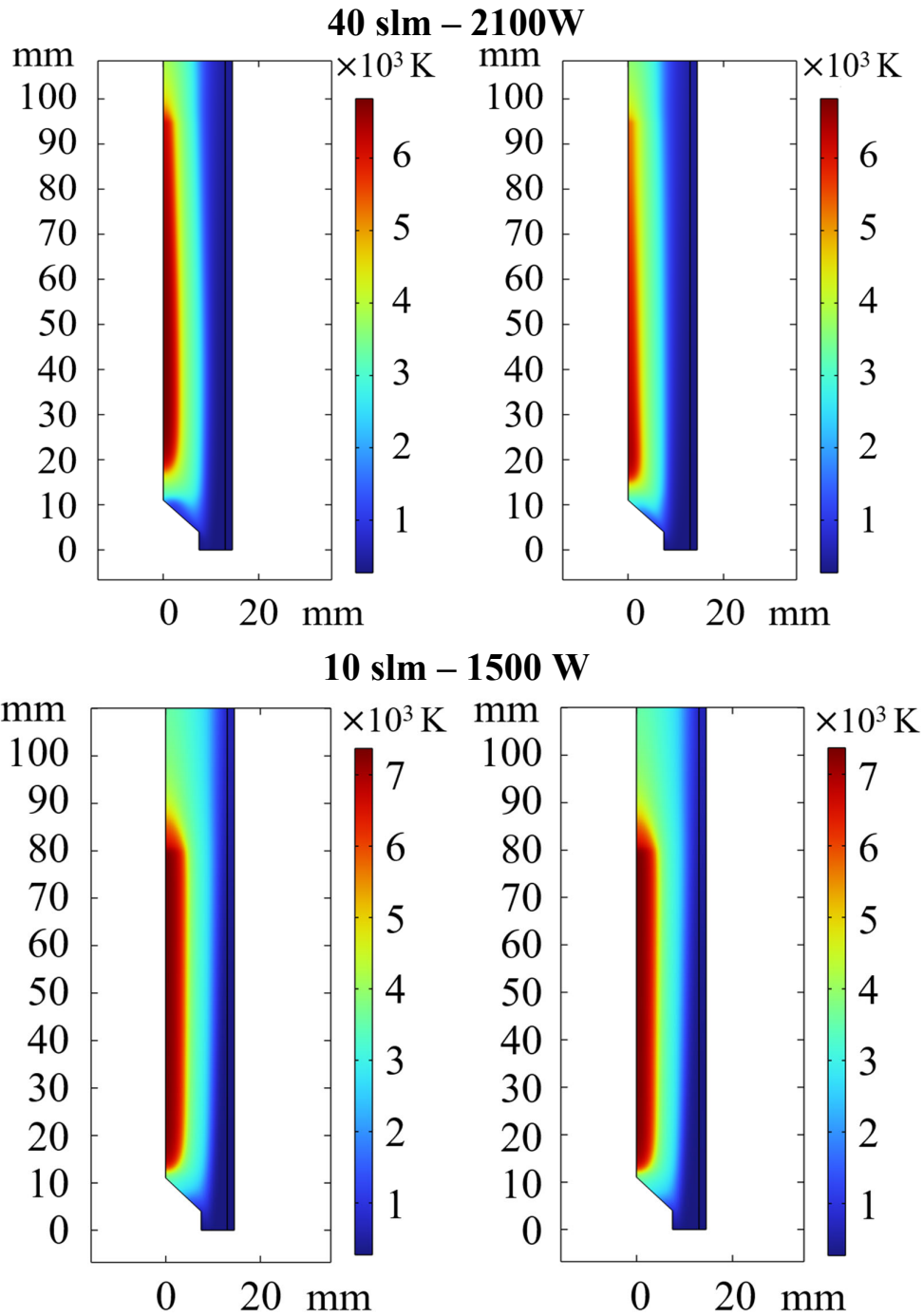


Figure S.13. Comparison of temperature profile for fixed values of  $k$  and  $\omega$  (left) and for the interpolated values (right), for 40 slm and 2100 W (top) and for 10 slm and 1500 W (bottom).

As can be seen in Figure S.13, when increasing the SEI at the highest flow rate (40 slm), the differences in temperature profile become less pronounced, whereas at the highest SEI condition and the lowest flow rate (10 slm), the differences are completely negligible.

All conclusions in the main paper are thus valid for both values of the turbulent kinetic energy and the specific dissipation rate at the inlet. The fixed values for turbulent kinetic energy and specific dissipation rate are used in the main paper, since computationally, they converge to a solution more easily.

### S.10 There is no chemical equilibrium and LTE in CO<sub>2</sub> MW plasma: Need for coupling all physics within the model

In LTE, the plasma's local composition depends solely on temperature and pressure [15, 16]. To evaluate the validity of the LTE approximation, we disregarded transport of species in our model, for the same gas flow velocity and temperature profiles, and hence, the temperature and pressure are kept identical. Diffusion is neglected by reducing all diffusion coefficients (cf. equation 12) to 1% of their original value, while turbulent diffusion is neglected by setting the turbulent Schmidt number (cf. equation 18) to  $10^6$  (the turbulent Schmidt number of a single species does not exceed 1.7 in any of the modelled conditions), and finally convective transport of species is ignored by setting the gas velocity in equation 8 to zero.

Figure S.14 shows the calculated mole fractions of the various species, when solving the thermochemical model (solid) and when neglecting transport (dashed), on a radial cutline taken at an axial position of 55 mm (i.e., the plasma center), for 1200 W, 10 slm and 1 atm. Note that the exact axial position for analyzing the molar fractions is not important, as long as it is within the plasma core, since the gradients in the z-direction are negligible, at least when we assume a rectangular function for the heat source along the axial direction. However, the gradients in the z-direction become important in the afterglow region.

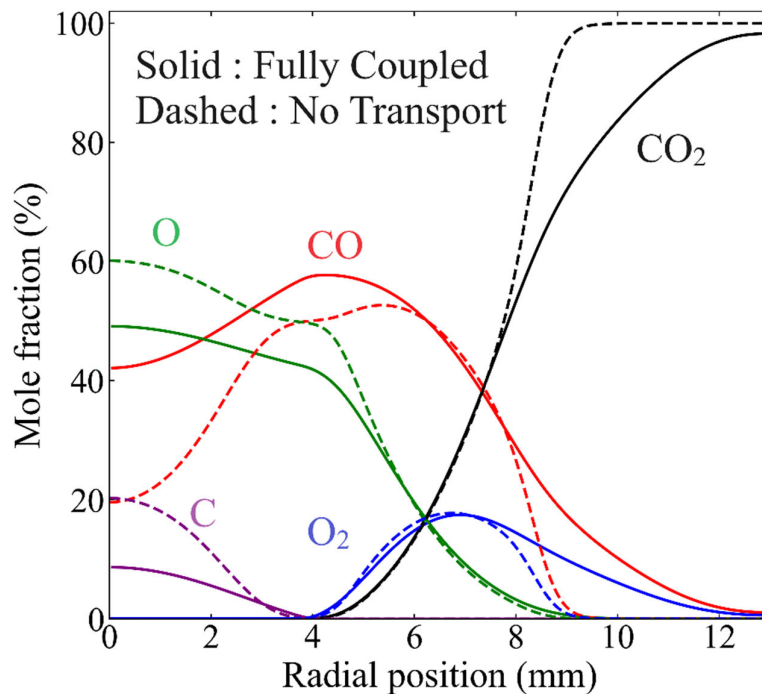


Figure S.14. Comparison of calculated molar fractions of the various plasma species along a radial cut line at  $z = 55$  mm, for 1200 W, 10 slm and 1 atm, for a solution where all physics considered in the model are fully coupled of the model (solid) and when transport of species is neglected (dashed).

As discussed above, within the LTE approximation, the local plasma composition does not depend on the transport of species. However, Figure S.14 shows that when transport of species is neglected, the molar concentration profiles differ strongly from the solution where all physics considered in the model are fully coupled. Consequently, LTE is not obtained, due to deviations in chemical equilibrium.

Indeed, to achieve chemical equilibrium in a CO<sub>2</sub> plasma, transport (predominantly diffusion) processes must be significantly slower than the reaction kinetics. When the total rate of all forward reactions in

which a species participates, is identical to the total rate of all backward reactions, chemical equilibrium is obtained. However, if the formed species is transported away before the backward reaction can take place, no chemical equilibrium is obtained. Hence, the difference between the solid and dashed lines in Figure S.14, i.e., with and without transport of species, clearly demonstrates that transport is important, and fast enough to disrupt chemical equilibrium.

Diffusion is fast enough to disrupt chemical equilibrium in the MW CO<sub>2</sub> plasma, because the large temperature gradient along the radial direction (cf. 6(a) of the main paper) results in large concentration gradients, promoting diffusion. Only between 6 and 8 mm, the LTE mole fractions correspond roughly with the mole fractions obtained with the solution where all physics considered in the model are fully coupled. However, as will be illustrated in section Figure S.15 below, there is still net production and transport in this region, indicating that also here chemical equilibrium is not obtained. In summary, it is clear that solving the transport of species, which drives the chemical non-equilibrium, is key in accurately assessing the CO<sub>2</sub> conversion. In the next section, we will evaluate the importance of transport by diffusion vs convection.

This discrepancy in mole fractions is sufficient evidence that LTE is not valid, and the influence of transport phenomena on the net rates, that are discussed in section 3.5 and 3.6 of the main paper, might not be as apparent.

Therefore, Figure S.15 shows the different components governing conservation of mass (cf. equation 8 of the main paper) of CO for steady state conditions, when neglecting transport, as a function of radial position, for an axial position of 55 mm (i.e., the plasma center). As transport phenomena are not taken into account, only the net reaction rates are plotted, because the net diffusive and convective flux of CO are zero. This figure should be compared with Figure 9 in the main paper, where transport is taken into account.

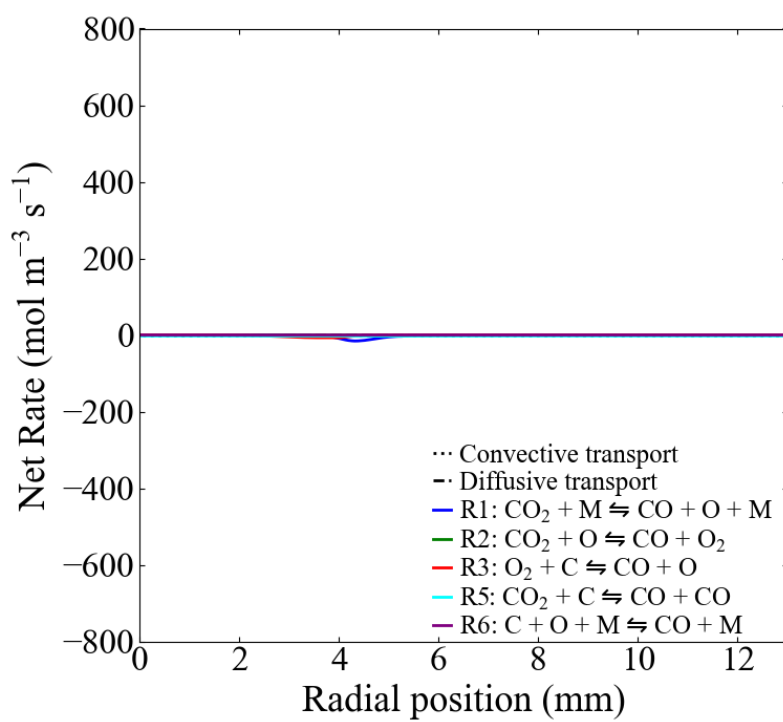


Figure S.15. Calculated net reaction rates of reactions involving CO atoms, neglecting transport, as a function of radial position, at an axial position of 55 mm, for 10 slm, 1200 W and 1 atm. The sign of the reaction rates is chosen so that positive values correspond to **net** CO production. The scale of the y-axis is kept the same as in Figure 9, for a 1-on-1 comparison.

As is apparent from Figure S.15, chemical equilibrium is reached when transport phenomena are neglected, because the net reaction rates are (close to) zero. There are very small deviations from zero, due to the numerically small diffusion. Moreover, by comparing to Figure 9 in the main paper, it is clear that species transport, mainly diffusion, is important in determining local net production rates.

### S. 11 Flow velocity lines and velocity components

Figure S.16 shows the flow lines in 3D across the 2D axisymmetric domain, with the temperature plotted on a cut plane through the center, for 10 slm, 1200 W and 1 atm.

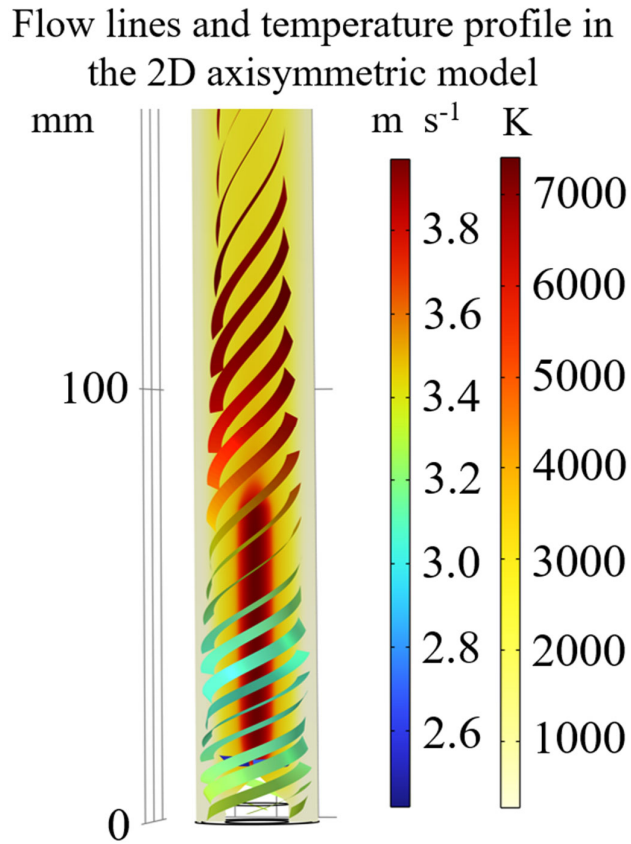
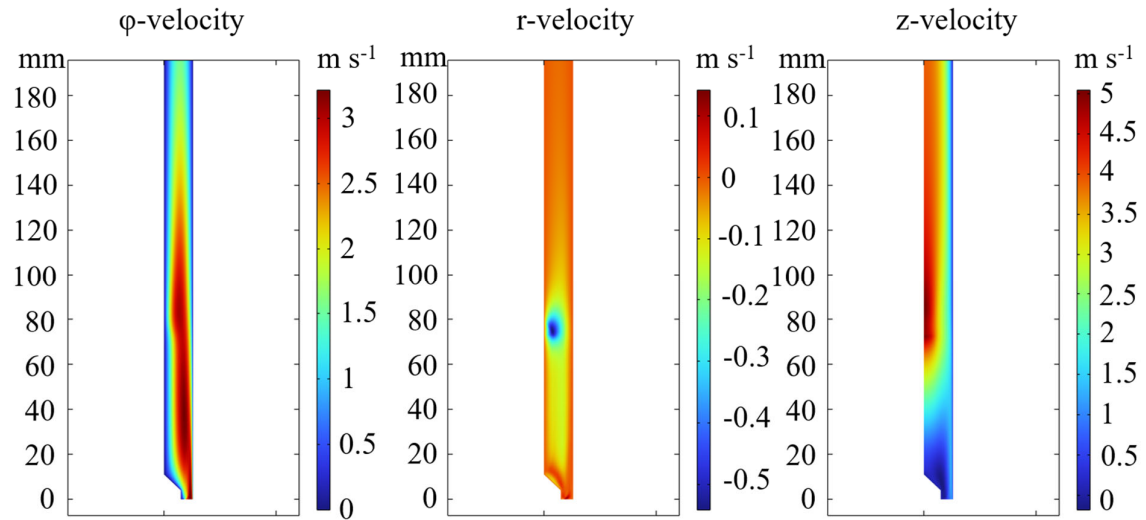


Figure S.16. Flow lines with uniform density and the temperature profile for 10 slm, 1200 W and 1 atm.

The flow lines are spaced with uniform density, and the figure illustrates that the flow speeds up after the plasma and that the swirl is maintained after the plasma. Figure S.17 depicts the different velocity components for 10 slm, 1200 W and 1 atm.



**Figure S.17.** Velocity components for 10 slm, 1200 W and 1 atm.

As can be seen in Figure S.17, the swirl flow is still present even after the plasma, and the z-velocity in the reactor is almost exclusively positive. Most importantly, the r-velocity is exclusively negative in the reactor, apart from a small region near the inlet. Hence, all convective transport is towards the symmetry axis of the reactor.

### S.12 Mole fraction analysis

Figure S.18 shows the difference in CO mole fraction between the laminar and turbulent flow solution, near the reactor outlet. Positive values mean a higher CO mole fraction in the laminar flow solution, while negative values correspond to a lower CO mole fraction.

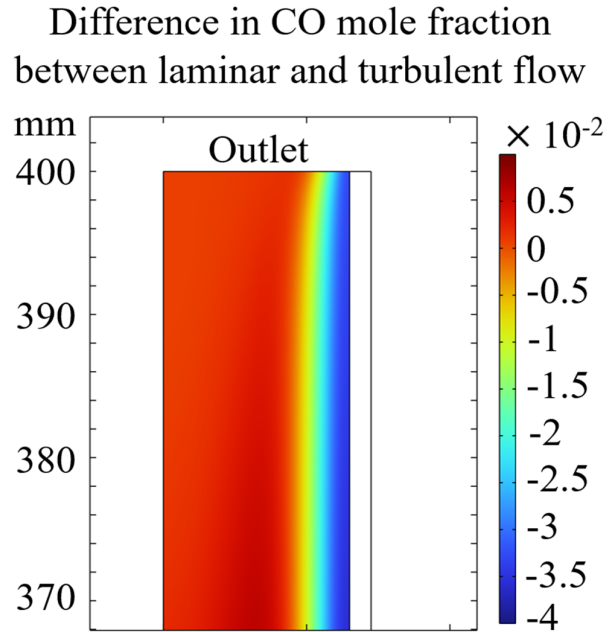


Figure S.18. Difference in mole fraction of CO between the laminar and turbulent solution near the outlet, at 1500 W, 40 slm and 1 atm.

Only at the edge of the fluid domain, there is significantly less CO present in the laminar solution (about 4%), and this result is a direct consequence of turbulent mixing at the edge of the domain. Turbulent diffusion causes more CO to diffuse into the cold gas stream at the edge of the reactor, where it can be transported out by axial convection.

### S.13 Bibliography

- [1] F. D'Isa, E. Carbone, A. Hecimovic, U. Fantz, Performance analysis of a 2.45 GHz microwave plasma torch for CO<sub>2</sub> decomposition in gas swirl configuration, *Plasma Sources Science and Technology* (2020). <https://doi.org/10.1088/1361-6595/abaa84>.
- [2] COMSOL, Comsol Multiphysics 6.0 CFD Module User's Guide.
- [3] S. Van Alphen, A. Hecimovic, C.K. Kiefer, U. Fantz, R. Snyders, A. Bogaerts, Modelling post-plasma quenching nozzles for improving the performance of CO<sub>2</sub> microwave plasmas, *Chemical Engineering Journal* 462 (2023) 142217. <https://doi.org/https://doi.org/10.1016/j.cej.2023.142217>.
- [4] K. Wang, S. Ceulemans, H. Zhang, I. Tsonev, Y. Zhang, Y. Long, M. Fang, X. Li, J. Yan, A. Bogaerts, Inhibiting recombination to improve the performance of plasma-based CO<sub>2</sub> conversion, *Chemical Engineering Journal* 481 (2024) 148684. <https://doi.org/https://doi.org/10.1016/j.cej.2024.148684>.
- [5] V. Kotov, C.K. Kiefer, A. Hecimovic, Validation of the thermo-chemical approach to modelling of the CO<sub>2</sub> conversion in sub-atmospheric pressure microwave gas discharges, *Plasma Sources Science and Technology* (2024).
- [6] D.C.M. van den Bekerom, J.M.P. Linares, T. Verreycken, E.M. van Veldhuizen, S. Nijdam, G. Berden, W.A. Bongers, M.C.M. van de Sanden, G.J. van Rooij, The importance of thermal dissociation in CO<sub>2</sub> microwave discharges investigated by power pulsing and rotational Raman scattering, *Plasma Sources Science and Technology* 28(5) (2019) 055015. <https://doi.org/10.1088/1361-6595/aaf519>.
- [7] J. Hildebrand, K. Hecht, J. Bliedtner, H. Müller, Laser Beam Polishing of Quartz Glass Surfaces, *Physics Procedia* 12 (2011) 452-461. <https://doi.org/https://doi.org/10.1016/j.phpro.2011.03.056>.
- [8] A.J. Wolf, F.J.J. Peeters, P.W.C. Groen, W.A. Bongers, M.C.M. van de Sanden, CO<sub>2</sub> Conversion in Nonuniform Discharges: Disentangling Dissociation and Recombination Mechanisms, *Journal of Physical Chemistry C* 124 (2020) 16806-16819.
- [9] B. Barnes, W. Forsythe, E. Adams, The total emissivity of various materials at 100–500° C, *JOSA* 37(10) (1947) 804-807.
- [10] F. Menter, M. Kuntz, R.B. Langtry, Ten years of industrial experience with the SST turbulence model, *Heat and Mass Transfer* 4 (2003).
- [11] F. Menter, Zonal Two Equation k- $\omega$  Turbulence Models For Aerodynamic Flows, 23rd Fluid Dynamics, Plasmadynamics, and Lasers Conference. <https://doi.org/10.2514/6.1993-2906>.
- [12] B.J. McBride, M.J. Zehe, S.D. Gordon, NASA Glenn Coefficients for Calculating Thermodynamic Properties of Individual Species, 2002.
- [13] P.D. Neufeld, A.R. Janzen, R.A. Aziz, Empirical Equations to Calculate 16 of the Transport Collision Integrals  $\Omega(l, s)^*$  for the Lennard-Jones (12–6) Potential, *The Journal of Chemical Physics* 57(3) (1972) 1100-1102. <https://doi.org/10.1063/1.1678363>.
- [14] L. Vialetto, A.W. van de Steeg, P. Viegas, S. Longo, G.J. van Rooij, M.C.M. van de Sanden, J. van Dijk, P. Diomede, Charged particle kinetics and gas heating in CO<sub>2</sub> microwave plasma contraction: comparisons of simulations and experiments, *Plasma*

Sources Science and Technology 31(5) (2022) 055005. <https://doi.org/10.1088/1361-6595/ac56c5>.

[15] A.B. Murphy, Thermal plasmas in gas mixtures, Journal of Physics D: Applied Physics 34(20) (2001) R151. <https://doi.org/10.1088/0022-3727/34/20/201>.

[16] M.I. Boulos, P.L. Fauchais, E. Pfender, Fundamental Concepts in Gaseous Electronics, in: M.I. Boulos, P.L. Fauchais, E. Pfender (Eds.), Handbook of Thermal Plasmas, Springer International Publishing, Cham, 2023, pp. 139-180. [https://doi.org/10.1007/978-3-030-84936-8\\_4](https://doi.org/10.1007/978-3-030-84936-8_4).